LA-7099-T
Thesis

UC-34
Issued: January 1978

A Theoretical Assessment of Radiation Damage Effects in a Proposed Gamma-Ray Laser System

Harold R. Schwenn*

*Visiting Staff Member.
Rensselaer Polytechnic Institute, Troy, NY 12181.

los alamos
scientific laboratory
of the University of California
LOS ALAMOS, NEW MEXICO 87545

UNITED STATES
DEPARTMENT OF ENERGY
CONTRACT W-7405-ENG. 36

This thesis was accepted by the Graduate Faculty of Rensselaer Polytechnic Institute, Troy, New York, in partial fulfillment of the requirements for the degree of Master of Science. It is the independent work of the author and has not been edited by the Technical Information staff.

Printed in the United States of America. Available from
National Technical Information Service
U.S. Department of Commerce
5285 Port Royal Road
Springfield, VA 22161

Microfiche	$ 3.00	126-150	7.25	251-275	10.75	376-400	13.00	501-525	15.25
001-025	4.00	151-175	8.00	276-300	11.00	401-425	13.25	526-550	15.50
026-050	4.50	176-200	9.00	301-325	11.75	426-450	14.00	551-575	16.25
051-075	5.25	201-225	9.25	326-350	12.00	451-475	14.50	576-600	16.50
076-100	6.00	226-250	9.50	351-375	12.50	476-500	15.00	601-up	--[1]
101-125	6.50								

[1] Add $2.50 for each additional 100-page increment from 601 pages up.

CONTENTS

LIST OF TABLES

LIST OF FIGURES

ABSTRACT

This paper is addressed to the question of the feasibility of pumping a gamma-ray laser (graser) with a nuclear explosion; in particular, to the problem of estimating the reduction of the cross section for stimulated emission, σ_{se}, caused by radiation damage associated with neutron pumping, as far as this can be determined from present understanding of the effects of radiation damage on the Mössbauer effect. The damage associated with neutron pumping of a graser is assessed in terms of the radiation damage model proposed by Kinchin and Pease. Expressions are derived for the damage concentration, both static and dynamic, for the energy deposited as heat per primary knock-on atom, and for the temperature rise due to a flux of neutrons in a hypothetical graser crystal, assuming certain models for heat flow. The mechanisms by which radiation damage affects the Mössbauer process are studied, with a review of the literature serving as a basis for empirical assessments of radiation damage effects upon the Mössbauer effect. To summarize the effects of radiation damage upon the contributing parameters, the stimulation cross section in a radiation damaged material, σ'_{se}, is written as a product of three reduction factors with σ_{seo}, the stimulation cross section in an undamaged material. With the expressions developed and assuming reasonable values for the contributing parameters, the maximum allowable temperature rise of the graser body and the maximum allowable average neutron energy of the pumping flux are derived. It is found that the flux requirements for pumping to inversion are more stringent than the limitations upon the flux due to radiation damage considerations. It is concluded that a graser system is more sensitive to the nuclear parameters of the graser material than to radiation damage effects and that radiation damage diminishes σ_{se} least in a monatomic metal.

PART 1

INTRODUCTION

As laser technology progressed, the possibility of observing stimulated emission of gamma radiation was considered. The first investigations into the feasibility of a gamma-ray laser (graser) came in the early 1960's.[1-5] At this time the problems associated with achieving stimulated resonant emission of gamma radiation seemed insurmountable, and interest in the subject reached its nadir through the late 1960's.

In the early 1970's interest was renewed, particularly in the U.S.S.R., as evidenced by the numerous papers that have appeared since 1971 dealing with the subject.[6-13] Until recently in the United States, work on this subject has been pursued for the most part by G. C. Baldwin[14-19] and the group from Livermore, L. Wood et al.[20-21]

Gol'danskii and Kagan[6] have proposed the use of a nuclear explosion to supply the intense neutron pulse required to pump a graser. As the graser depends upon the Mössbauer effect to achieve resonant emission, and the Mössbauer effect depends upon crystal perfection and temperature, radiation effects concomitant with the pumping process--disruption of crystal perfection and heating--must be considered. The compatibility of the pumping process with the requirements of the stimulated emission process are central to any discussion of grasers. In an attempt to determine the feasibility of pumping a graser with a nuclear explosion, this thesis is addressed to an examination of the radiation effects arising from neutron scattering and how these effects may be expected to affect the resonant emission process.

PART 2

PRINCIPLES OF GRASER OPERATION AND IMPLICATIONS

2.1. Basic Principles

The requirement for gamma-ray amplification by stimulated emission of radiation is

$$N_2\sigma_{se} - N_1\sigma_{ra} > \mu \quad , \tag{1}$$

which may be written as (see below)

$$N^*\sigma_{se} > \mu \quad , \tag{1a}$$

where N_2 = population of upper level,
N_1 = population of lower level,
g_2/g_1 = statistical weight factor,
N^* = population inversion $\equiv N_2 - (g_2/g_1)N_1$,
σ_{se} = cross section for stimulated emission,
σ_{ra} = cross section for resonant absorption,
μ = nonresonant removal coefficient.

This relation states that more photons must be added to the photon field by stimulated emission than are removed by resonant and nonresonant processes. Relation (1a) follows from relation (1) because the cross section for stimulated emission, σ_{se}, is equal (except for a statistical weight factor) to the cross section for the inverse process, resonant absorption. As resonant absorption (and emission) of recoilless gamma radiation is the Mössbauer effect, its inverse, stimulated emission of recoilless gamma radiation, corresponds to the Mössbauer effect in a medium in which there exists a population inversion. Thus, to consider the effect of radiation damage upon the cross section for stimulated emission, the effect of radiation damage upon the parameters of the Mössbauer effect is studied.

2.2. Achieving the Population Inversion

According to the Gol'danskii-Kagan proposal,[6] population inversion is achieved by using the moderated neutron flux originating from a nuclear explosion to transmute a parent nuclide to an excited state of the transmuted nuclide: ${}^{A}_{Z}X(n,\gamma){}^{A+1}_{Z}X^{**}$. The population inversion then occurs between the excited nuclide (${}^{A+1}_{Z}X^{**}$) and a lower excited state of this nuclide (${}^{A+1}_{Z}X^{*}$) or the ground state (${}^{A+1}_{Z}X$). This process is shown in Fig. 1.

The minimum number of capture events has been estimated to be not less than 10^{18}-10^{19} cm^{-3} for resonant photon energies of 10-100 keV.[6] Even assuming a very high radiative-capture cross section for the parent nuclei [$\sigma_{n\gamma}$ (thermal) $\sim 10^4$ barn] and neutron energies of $\sim$ 100 eV, an integrated neutron flux of the order of 10^{19}-10^{20} cm^{-2} would be required; and this must be delivered in a time short compared to τ, the natural lifetime of the excited state.

2.3. Time Dependence of the Resonance Cross Section

Lynch et al.[22] have observed that the cross section for resonant absorption, σ_{ra}, is time dependent. As σ_{se} is proportional to σ_{ra}, it is to be expected that σ_{se} is also time dependent. Quantum mechanical considerations lead to the same conclusion.[1,23] The time-dependent cross section for stimulated emission is

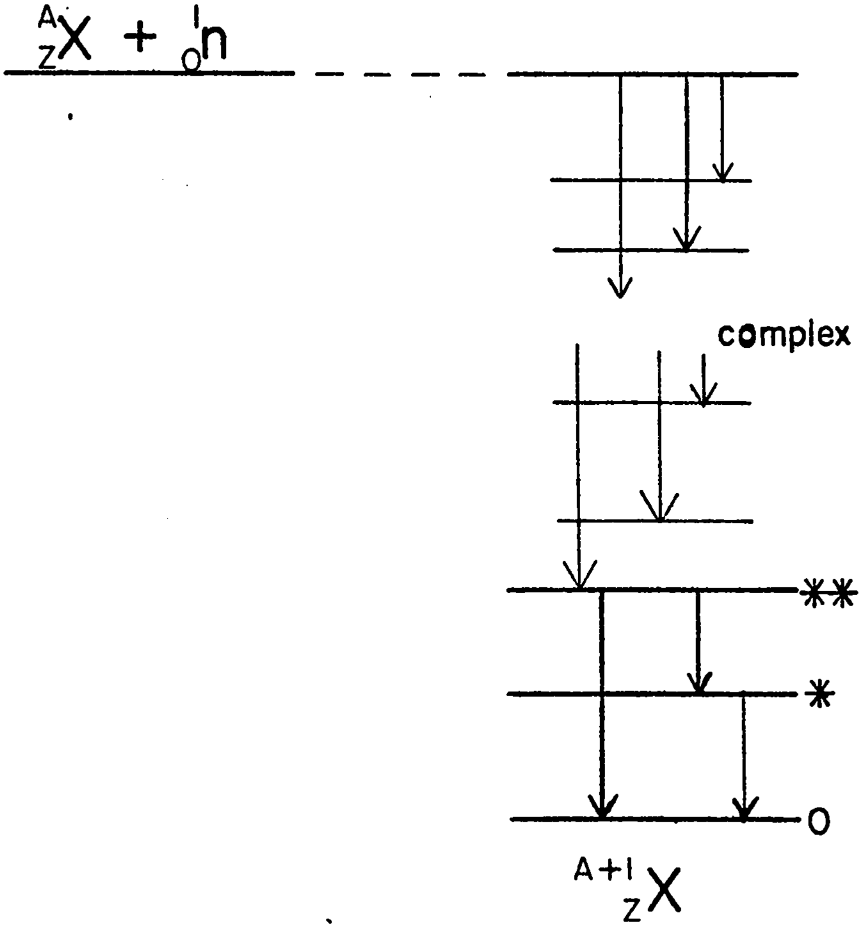

Figure 1. Proposed method for achieving population inversion and transitions that may be used.

$$\sigma_{se}(t) = \frac{\Lambda^2}{2\pi} \frac{\beta f}{(1+\alpha)} \frac{1}{\tau} \frac{1}{A(t)} \int_0^t A(t')dt' \xrightarrow[\lim\, t\to\infty]{} \frac{\Lambda^2}{2\pi} \frac{\beta f}{(1+\alpha)} \frac{1}{\tau} \frac{\hbar}{\Gamma} \quad , \qquad (2)$$

where Λ = wavelength,

β = branching ratio,

f = recoilless fraction,

τ = natural lifetime,

Γ = linewidth,

α = internal conversion coefficient.

$A(t)$, the vector potential of the wave, is given by

$$\frac{\partial A}{\partial x} = - \frac{\mu A}{2} + \frac{N^* \sigma_a \Gamma}{2} \int_0^t A(t')dt' \quad , \qquad (3)$$

where x = position in direction of propagation of the beam,

μ = nonresonant removal coefficient,

σ_a = asymptotic value of the stimulated emission cross section.

Estimated values for these parameters are shown in Table I.

TABLE I

EVALUATION OF σ_a FROM TYPICAL VALUES OF THE CONTRIBUTING PARAMETERS

E (keV)	6.0	10.0	15.0
Λ (Å)	2.07	1.24	.828
β	1.	1.	1.
f	1.	1.	1.
α	20.	20.	20.
$\frac{\Lambda^2}{2\pi} \frac{\beta f}{(1+\alpha)}$ (barns)	3.25(6)	1.17(6)	5.20(5)

The nonresonant removal coefficient, $\mu = N\sigma_{NRA}$ where σ_{NRA} is the nonresonant absorption cross section, depends upon the photon energy and the material. Beryllium, iron, and tantalum have been chosen as examples of low, medium, and high-Z materials. The nonresonant absorption cross sections at selected energies are given in Table II.

TABLE II

σ_{NRA} FOR Be, Fe, AND Ta AT 6, 10, AND 15 keV

E (keV)	6.	10.	15.
σ_{NRA} (Be) (barns)	37.2	7.92	3.56
σ_{NRA} (Fe) (barns)	7,110.	15,700.	5,060.
σ_{NRA} (Ta) (barns)	100,000.	72,400.	39,100.

For the case of Ta in a Be host, as considered in Ref. 6, the required inversion density is

$$N^* > \frac{\mu}{\sigma_a} = \frac{N\sigma_{NRA}}{\sigma_a} = 1.8\ [18]\ ,$$

where the Be host is considered to be doped to a concentration of 10^{-4}.

It follows from relation (1a) that lasing action cannot occur until σ_{se} has attained a value large enough to establish the inequality of relation (1a). This implies that there is a time lag between the establishment of the population inversion and the onset of laser action. This time lag is of the order of τ; thus, a fundamental time scale for lasing is established.

As a consequence of the lag in σ_{se} (as will be shown later), one need only to consider the radiation effects upon the asymptotic value of σ_{se} and not the exact time variation of these effects. Examination of

Eq. (2) shows that the asymptotic value of σ_{se} goes as f/Γ, since, for a given isomer, all other parameters in σ_{se} are fixed. Therefore, anything that reduces f or increases Γ will reduce the asymptotic value of σ_{se}. Radiation effects do both.

PART 3

MÖSSBAUER EFFECT

3.1. The Recoilless Fraction

Recoilless emission and absorption of gamma radiation are most easily understood by considering the quantum mechanical properties of a crystalline solid. The crystal lattice to which the emitting (or absorbing) nucleus is bound has a quantized vibrational spectrum that allows nuclei only discrete states of excitation of the 3N vibrational modes. The recoil momentum of the emitting (or absorbing) nucleus delivers an impulse to the crystal. This impulse does not necessarily cause a change of the vibrational energy state of the crystal. The gamma rays resulting from these zero-phonon events have the full energy of the nuclear transition, and therefore, the proper energy to be resonantly absorbed or to stimulate resonant emission—as the case would be in an inverted medium.

The fraction of all emission (or absorption) events that are unaccompanied by phonon exchange, known as the recoilless fraction, f, is given by

$$f = \exp(-\langle x^2 \rangle / \lambda\!\!\!^{-2}) \quad , \tag{4a}$$

where $\langle x^2 \rangle$ = the mean square deviation of the vibrating atom from its equilibrium position,

$\lambda\!\!\!^{-}$ = $\lambda/2\pi$,

λ = the wavelength of the emitted photon.

For the Debye model of lattice vibrations Eq. (4a) takes the particular form

$$f = \exp - \left\{\frac{3E^2}{Mc^2k\theta}\left[\frac{1}{4} + \left(\frac{T}{\theta}\right)^2 \int_0^{\theta/T} \frac{x\,dx}{e^x-1}\right]\right\} , \qquad (4b)$$

where E = the energy of the nuclear transition,

M = the mass of the emitting (or absorbing) nucleus,

c = the speed of light,

k = the Boltzman constant,

θ = the Debye temperature of the crystal,

T = the absolute temperature of the crystal.

Equation (4b) should be used with some care as the Debye model from which it is derived treats the lattice as a structureless continuum, and as such, does not account for deviations arising from lattice type or other structure related effects.

3.2. Linewidth

3.2.1. The Natural Linewidth

In Fig. 2 a recoilless emission event is represented by transition A, while transition B represents an emission event accompanied by recoil.

If several recoilless emission events occur and $E_{10} = E_{10}' = E_{10}''$, etc., then a Mössbauer spectrum of natural linewidth is observed. If, however, $E_{10} \neq E_{10}' \neq E_{10}''$, etc., then the recoilless emission is inhomogeneously broadened. In this case, it is not the energy of the

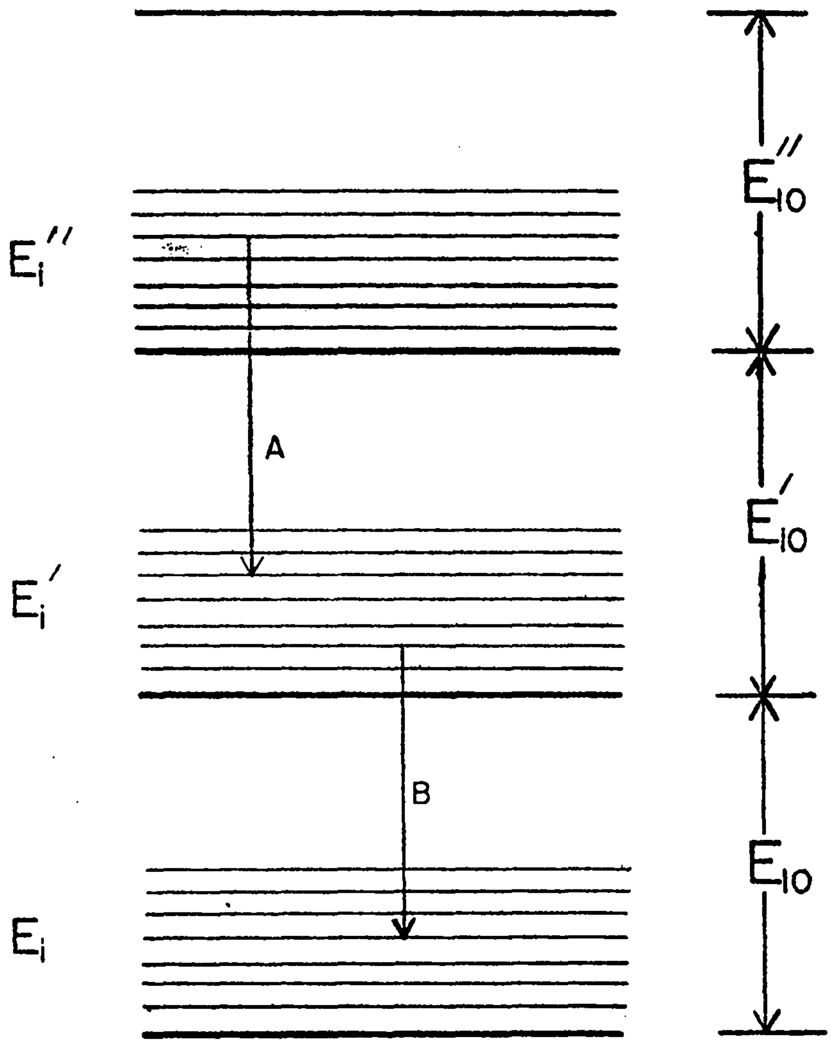

Figure 2. An energy diagram (not to scale) of a crystal in which several nuclei in the crystal may be excited. E_{10} is the nuclear excitation energy of these nuclei. (Typically for the Mössbauer effect, this is the energy difference between the ground state and the first excited state.) The closely spaced states, denoted by E_i, represent the vibrational energy levels of the crystal. Transition A represents a recoilless emission process. The vibrational energy state of the crystal has not changed, $E_i' = E_i''$, thus the photon carries off the full energy of the transition, E_{10}'. A nonrecoilless emission process is represented by B, $E_i' \neq E_i$.

individual photon that is broadened (this is not possible), but the distribution of the energies of the individual transitions from which the photons arise.

In an ideal case, the observed linewidth, Γ, equals the natural linewidth, Γ_n, which is determined by the Heisenberg uncertainty principle, $\Delta E \Delta t \geqslant \hbar$. The uncertainty in time is equal to the natural lifetime of the state, τ, from which it follows that the minimum width in energy is $\Delta E = \frac{\hbar}{\tau} = \Gamma_n$.

3.2.2. Increased Linewidth Due to Shifts of Line Frequency

The observed transition energy, E, will differ from the expected transition energy, E, if there are perturbations of the nuclear levels. These perturbations arise from the second-order Doppler shift, gravitational shift, isomer shift, or hyperfine interactions. The second-order Doppler shift and the gravitational shift may be ignored if it is assumed that there are no temperature gradients or gravitational potential gradients across the graser crystal. The gravitational shift is unaffected by radiation effects. Temperature gradients may be induced by nonuniform (radiation induced) heating; however, the model used in this thesis assumes uniform heating. Therefore, in this model, temperature gradients are assumed not to exist, and the second-order Doppler shift may be neglected. The isomer shift and hyperfine interactions are affected by radiation effects and, therefore, must be studied in more detail.

The isomer shift arises from the electrostatic (monopole) interaction of nuclear and electronic charges. It is given by the equation:

$$\text{isomer shift} = \frac{2}{3}\pi Z e^2 \{ |\psi_a(o)|^2 - |\psi_s(o)|^2 \} \delta \langle r^2 \rangle \quad , \qquad (5)$$

where $|\psi_a(o)|^2$ is the electron charge density at the absorbing nucleus, $|\psi_s(o)|^2$ is the electron charge density at the source nucleus, and $\delta\langle r^2\rangle$ is the difference between the mean square nuclear charge radii of the excited (source) and ground (absorber) states. In the case of the graser, Eq. (5) would be written as

$$\text{isomer shift} = \tfrac{2}{3}\pi Ze^2\{|\psi_{re}(o)|^2 - |\psi_s(o)|^2\}\delta\langle r^2\rangle \quad , \tag{5a}$$

where $|\psi_{re}(o)|^2$ is the electron density at the resonantly emitting nucleus. Thus, a variation of the electron charge density throughout the crystal causes an isomer shift between a source nucleus and other nuclei with which it would otherwise be in resonance.

The hyperfine interactions include any higher order electric or magnetic interactions. Typically, interest is limited to the electric quadrupole and magnetic dipole interactions. These interactions split the degeneracy of the nuclear energy levels according to the following equations:

$$E_Q = \frac{\phi_{zz}eQ}{4I(2I-1)} \;[3m_i^2 - I(I+1)]\ldots \quad , \tag{6}$$

for the electric quadrupole interaction in an axially symmetric field, and

$$E = -\mu H m_i/I \quad , \tag{7}$$

for the magnetic dipole interaction. In these relations,

ϕ_{zz} = the second derivative of the electric potential in the axial direction;

e = the charge of an electron;

Q = the quadrupole moment of the nucleus;

I = the spin of the nucleus;

m_I = the magnetic quantum number = $-I, -I+1, \ldots I-1, I$;

H = the magnetic field;

μ = the magnetic moment of the nucleus.

When the degeneracies of the excited state and ground state are lifted by these interactions, the number of lines emitted is determined by the selection rules for nuclear transitions. These shifts and splittings lead to additional structure if their magnitudes are great enough to resolve the additional line or lines. They will lead to broadening if the shift or splitting is not large enough to be resolved, or if there is a distribution in values of the shift or splitting. This may arise from a variation in symmetry from point to point or region to region throughout the crystal. Such a variation may be caused by radiation damage.

3.2.3. Observations of Linewidths

Mössbauer spectra of natural linewidth may be obtained for isomers with short lifetimes ($< 10^{-8}$s) while Mössbauer spectra of isomers with long lifetimes ($> 10^{-7}$s) are always broader than the natural linewidth. This observation is best summarized by Fig. 3. This effect may arise from monopole interactions together with interactions of nuclear electric and magnetic moments with electromagnetic fields within the crystal. In a real crystal, naturally occurring inhomogeneities give

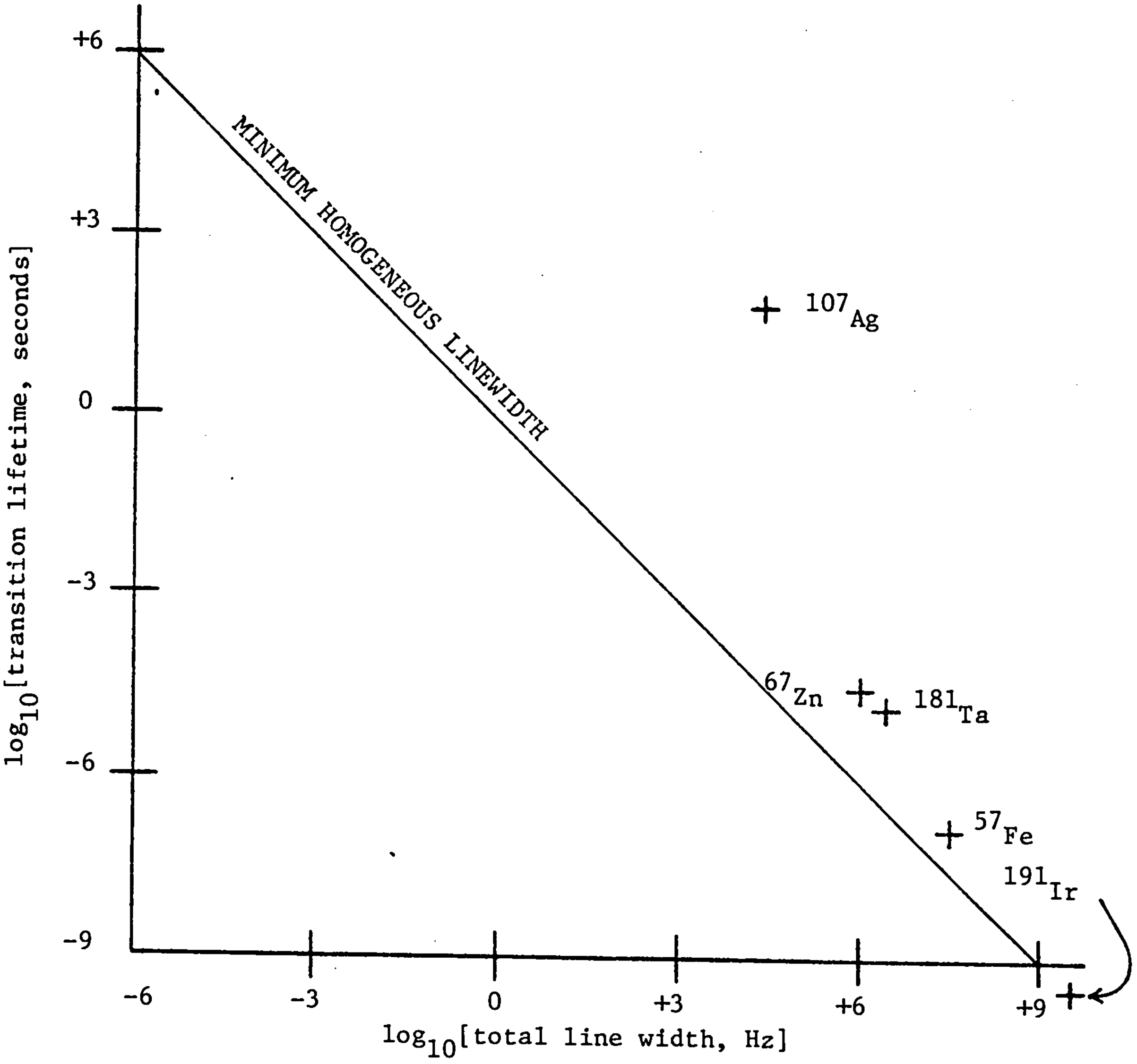

Figure 3. Transition lifetime versus total linebreadth shows that as the natural lifetime increases, the observed linebreadth diverges from the natural linebreadth and appears to approach an asymptotic value of ∿ 10^4 Hz. (Adapted from Ref. 19.)

rise to local variations of the crystalline fields, causing point-to-point perturbations of the Mössbauer line that can exceed Γ_n. Even in an ideal crystal, in which it is assumed there are no inhomogeneities of the crystal fields, variations in the spin-spin interaction arising from random orientations of the nuclear spins throughout the crystal (due to thermal agitation) would still broaden the line. For long-lived isomers, these otherwise minute perturbations dominate the line-width because Γ_n is so narrow.

PART 4

RADIATION DAMAGE

Radiation damage is essentially an alteration of the lattice structure (viz., point defects, displacement cascades, etc.) due to interactions between the radiation and the crystal. This alteration may be exhibited as a change in macroscopic properties; e.g., increase of electrical resistivity, decrease of thermal conductivity, hardening, swelling, etc. These macroscopic changes may be understood in terms of microscopic changes that result from exposure to radiation. In this thesis, all effects of concern originate from neutron interactions as, even in the immediate vicinity of a nuclear explosion, primary gamma radiation may be effectively shielded against.

4.1. Neutron Interactions

It is convenient to consider the neutrons as either slow or fast according to the following distinction. A slow neutron has an energy, E_n, given by

$$E_n < E_d/\Lambda,$$

where E_d = a sharply defined displacement energy of an atom in a crystal, taken to be 25 eV;

$\Lambda = 4A/(A+1)^2$;

A = the atomic weight of an atom of the crystal.

4.1.1. Slow Neutrons

Although the scattering of slow neutrons makes a small contribution to the heating, it does not damage the crystal directly. The damage caused by slow neutrons is the result of the (n,γ) reaction. When the neutron is captured, the capturing nucleus emits a cascade of gammas of approximately 5- to 8-MeV total energy, recoiling with an average energy of approximately 50 eV[24,25,26] -- just sufficient to produce a point defect in the immediate vicinity of the capturing nucleus. Thus the damage is correlated to the excitation.

4.1.2. Fast Neutrons

Besides heating, fast neutrons cause bulk damage. The scattering of fast neutrons is not necessarily correlated with the excitation mechanism. Two forms of fast neutron damage are conceivably of importance, i) static damage; and ii) dynamic damage.

i) Static damage is the long-lived alteration of the crystal following irradiation. It is the form of damage that is regularly investigated in radiation damage experiments. Although correlated point defects associated with the (n,γ) reaction are also a form of static damage, it is best to consider them separately due to the differences in the nature of the damage between that caused by fast neutrons and that caused by the (n,γ) process.

ii) Dynamic damage is that transient condition in which atoms are not merely off their lattice sites, but are still recoiling. It is caused by neutron scattering and the ensuing displacement cascade. It is possible within the limits of a model to calculate the average length of time that a knock-on is in motion before coming to rest (see Appendix A). Given this time, it is then possible to calculate the equilibrium concentration of atoms in motion at any given moment and assess their effect.

4.2. Radiation Damage Mechanisms

Three basic mechanisms have been proposed to explain radiation effects:

i) thermal spikes,
ii) displacement spikes,
iii) displacement cascades.

4.2.1. Thermal Spikes

The thermal spike may be envisioned as a sudden delivery of heat to a restricted volume of the lattice. When a collision with an atom imparts an energy less than E_d, this energy is dissipated by an increased vibrational amplitude about the lattice site. This increased amplitude of vibration is damped out by spreading of the excitation into the surrounding crystal. Although for very short times this is not an equilibrium process, it may be thought of as a localized high temperature that spreads out in time. Such temperature spikes enhance diffusion and other activated processes.

A thermal spike model to account for structural changes of materials following ion impact has been proposed by Kelly and Naguib.[27] Their results indicate that materials for which the ratio of the crystallization temperature to the melting temperature (T_c/T_m) is less than 0.29 show good radiation stability, while substances with $T_c/T_m > 0.29$ amorphize readily. A summary of irradiation effects upon several materials is presented in Table III. These results are based on evidence obtained from disorder-induced gas release and electron-diffraction pattern studies.

These techniques indicate bulk damage; thus, these results should be considered to pertain to bulk properties. Although this model is qualitatively successful, it does not lend itself to a quantitative characterization of the damage.

TABLE III

A SUMMARY OF IRRADIATION EFFECTS UPON SEVERAL MATERIALS*

Substances that show good radiation stability	Substances that readily amorphize under ion impact
CaO	Al_2O_3
Cr_2O_3	diamond
MgO	Fe_2O_3
NiO	GaAs
SnO_2	Ge
ThO_2	Si
UO_2	SiO_2
ZrO_2	Ta_2O_5
	TiO_2
	U_3O_8
	$ZrSiO_4$

---

*Adapted from Kelly and Naguib.[27]

4.2.2. Displacement Spikes

The displacement spike, first proposed by Brinkman,[28] differs from the thermal spike in that the knock-on atoms receive energies greater than E_d and the calculated[28] mean free path for displacement collisions is less than an interatomic distance. When this occurs, the primary knock-on displaces essentially every atom it encounters producing a large void-like region. The pattern of rearrangement is an inversion of the material in the spike, the atoms along the axis being driven outward most violently and ending up outside of those in the adjacent tubular region. Such a configuration is shown in Fig. 4.

In Brinkman's model, the atoms driven from the core of the spike end up in the surrounding tubular region. A very high temperature and pressure are associated with this configuration due to the increased atom density in the tubular region. This configuration is unstable and immediately collapses. The collapse, which is characterized by turbulent flow of this molten region, leaves the resolidified material for the most part congruent with the original lattice, while small misoriented regions and entangled dislocation loops characterize the remanent damage.

Seeger modified Brinkman's displacement spike concept[29] by taking the lattice periodicity into account. In Seeger's model, some of the atoms that are driven from the core of the spike do not end up nearby in the tubular region, but travel a rather large distance from the spike by means of a focused momentum transfer along a crystallographic direction, termed a "focuson," before coming to rest as interstitials. The configuration of this stage of the displacement spike consists of a vacant core surrounded by interstitials, some at great distance. When this configuration relaxes, not all of the interstitials

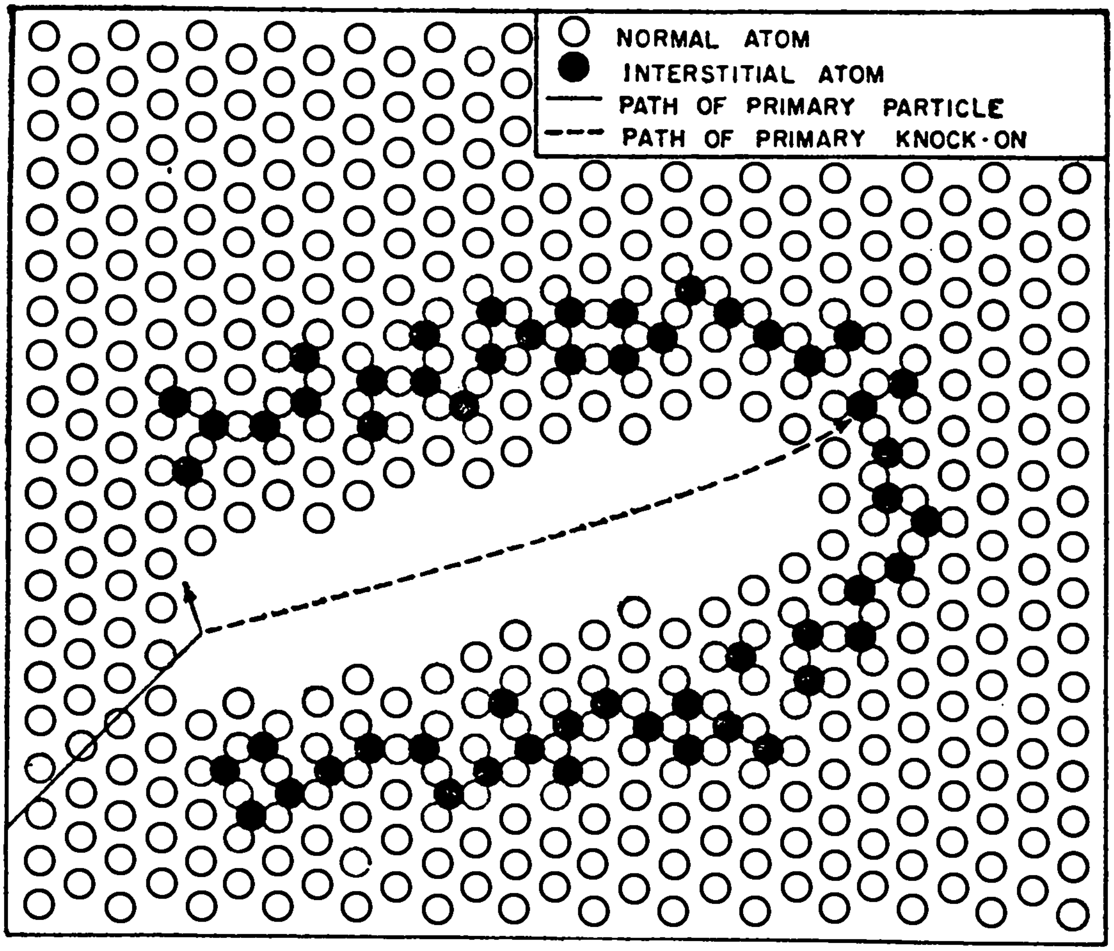

Figure 4. The pattern of rearrangement during production of a displacement spike. (From Ref. 34 where it is attributed to Ref. 28.)

return to the vacant region. The region of missing atoms at the center of the core is termed a depleted zone. This model of the displacement spike has the additional feature of a depleted zone surrounded by distant interstitials. These results are very similar to those envisioned for a displacement cascade.

4.2.3. Displacement Cascades

The displacement cascade may be envisioned as a branching sequence of binary collisions. An energetic PKA can collide with and displace a secondary knock-on atom. These in turn may displace other atoms in cascade fashion. Numerical calculations using a cascade model[30,31] indicate that the defect configuration comprises vacancy clusters with outlying interstitials. This is similar to the configuration predicted for a displacement spike; however, the displacement cascade is more amenable to numerical calculation.

4.3. Radiation Damage Models

The model for "The Displacement of Atoms in Solids by Radiation" proposed by Kinchin and Pease[32] has been chosen in order to calculate the expected temperature rise, concentration of long-lived defects (static damage), and measures of dynamic damage that result from the pumping process. This model produces essentially the same results as that of Snyder and Neufeld.[33] It is, however, generally accepted[34,35] that both models overpredict the number of displaced atoms by a factor of from 2 to 5. This conclusion is based primarily on results obtained from electrical resistivity measurements.

With these limitations in mind, these models give a good approximation of the damage to be expected from a given fluence of neutrons of a given energy. As there are no comprehensive theories relating the Mössbauer parameters to the defect concentration in a crystal, an ability to calculate the exact number of defects is not necessary. What is necessary is to be able to characterize the damage in a consistent manner so that a comparison with experimental results can be made. To this end, the model of Kinchin and Pease will be used.

4.3.1. Model of Kinchin and Pease

This model considers the effects of an atom moving through a solid. Three energy limits for collisions between the moving atom and the stationary atoms of the solid, L_A, L_B, and L_C, are considered. L_A defines that energy of the moving atom below which hard-sphere collisions are considered to occur and above which Rutherford collisions are considered to occur. L_B defines that energy of the moving atom below which all Rutherford collisions displace atoms and above which only some of the Rutherford collisions displace atoms. L_C defines the energy of the moving atom below which ionization losses may be neglected. If the moving atom has an energy greater than L_C, the energy lost in electronic excitation is far greater (by a factor of $\sim 10^3$) than that lost in any other process. Figure 5 illustrates the regimes in which the various mechanisms of energy loss predominate. These limits are given by the following expressions:

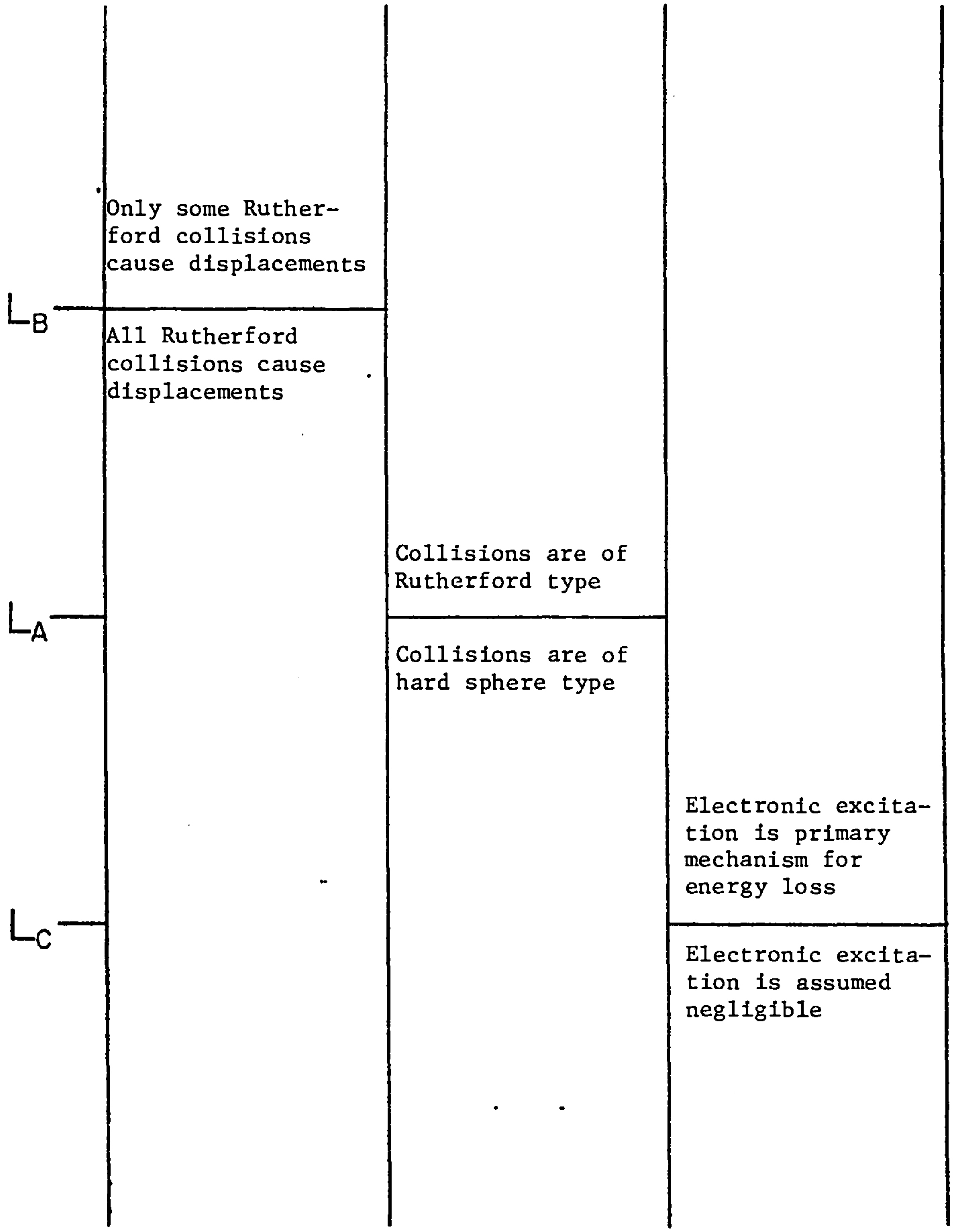

Figure 5. The energy regimes in which the various mechanisms of energy loss predominate. Numerical values of L_A, L_B, and L_C (the magnitudes of which are not necessarily in the order shown in this figure) are given in Table IV.

$$L_A = 2E_R Z_1 Z_2 \, (Z_1^{2/3} + Z_2^{2/3})^{1/2} \, (M_1 + M_2)/M_2 \quad , \tag{8a}$$

$$L_B = 4E_R^2 Z_1^2 Z_2^2 \, (Z_1^{2/3} + Z_2^{2/3}) \, M_1/M_2 E_d \quad , \tag{8b}$$

$$L_C = \begin{cases} 1/8(M_1/m) I_t \text{ for insulators,} \\ 1/16(M_1/m)\varepsilon_o \simeq 1/16(M_1/m)\pi a_o^2 E_R (3N_o\sqrt{\pi})^{2/3} \text{ for metals,} \end{cases} \tag{8c}$$

where E_R is the Rydberg energy (13.60 eV), Z and M are the atomic numbers and masses, respectively, and the subscripts 1 and 2 refer to the moving and stationary atoms, respectively. E_d was defined in Sec. 4.1. In the expressions for L_C, m is the mass of an electron and I_t (in the expression for insulators) is the lowest electronic excitation energy (corresponding to the edge of the first main band in the optical absorption spectrum). In the expression for metals, ε_o is the Fermi energy of the free electrons, a_o is the Bohr radius ($a_o = \hbar^2/me^2 = 5.29 \times 10^{-9}$ cm), and N_o is the number of atoms per unit volume.

Values of L_A, L_B, L_C, and of the minimum neutron energy required to produce a knock-on of this energy are given in Table IV for several materials.

4.3.2. Number of Displacements Generated by a Moving Atom

Consider a monatomic solid in which a primary knock-on of energy $E' < L_A$ has been produced. The primary and subsequent higher order knock-ons undergo hard-sphere collisions in coming to rest. Any atom of the solid that receives an energy greater than E_d as a result of a collision is displaced. The total number of displaced atoms resulting

TABLE IV

MINIMUM NEUTRON ENERGY, E_{nA}, E_{nB}, AND E_{nC}, REQUIRED TO CREATE KNOCK-ONS OF ENERGY L_A, L_B, AND L_C, RESPECTIVELY, FOR SEVERAL ATOMS IN SEVERAL MATERIALS

Material	Moving Atom	A	L_A	E_{nA}	L_B	E_{nB}	L_C	E_{nC}
Be	Be	9	2.0[3]	5.4[3]	3.8[4]	1.1[5]	9.4[3]	2.6[4]
Diamond	C	12	5.0[3]	1.8[4]	2.5[5]	8.9[5]	1.5[4]	5.3[4]
Al	Al	26	3.1[4]	2.1[5]	9.3[6]	6.6[7]	1.7[4]	1.2[5]
K	K	40	7.4[4]	7.8[5]	5.5[7]	5.8[8]	9.2[3]	9.7[4]
Fe	Fe	56	1.5[5]	2.2[6]	2.4[8]	3.4[9]	4.5[4]	6.6[5]
Cu	Cu	63	2.0[5]	3.2[6]	4.0[8]	6.4[9]	5.1[4]	8.3[5]
W	W	184	1.8[6]	8.2[7]	3.1[10]	1.5[12]	1.2[5]	5.7[6]
Au	Au	197	2.1[6]	1.0[8]	4.2[10]	2.1[12]	1.2[5]	6.0[6]

from a primary knock-on of energy E' and its subsequent knock-ons coming to rest is

$$\nu = E'/2E_d \text{ for } E' > 2E_d \quad , \tag{9}$$

$$\nu = 1 \qquad \text{for } 0 \leqslant E' \leqslant 2E_d \quad . \tag{10}$$

This result also holds for $L_A < E' < L_B$ provided $E' < L_C$. As shown in Table 4, $L_C < L_B$; therefore, Eqs. (9) and (10) are valid for all cases in which $E' < L_C$.

Since Eq. (9) is linear in E', it is also correct when E' is replaced by $\bar{E}$, where $\bar{E}$ represents the average energy of a group of primary knock-ons with average energy greater than $2E_d$. In this case, ν represents the number of atoms displaced, on the average, by each primary knock-on.

The case in which $E' > L_B$ need not be considered, since creation of a primary knock-on with energy $E' > L_B$ by neutron bombardment would require excessively high neutron energies for the cases to be considered.

The general case for $E' > L_C$ is not treated by Kinchin and Pease.[32] However, the case in which the primary knock-on is produced by neutron bombardment is considered in adequate detail.

4.3.3. Effects of Neutron Irradiation, According to Kinchin and Pease

If isotropic scattering (in the Center-of-Mass System) is assumed, the energy spectrum of the primary knock-on atoms, $N_p(E')dE'$, is given by the relation:

$$N_p(E')dE' = dE'/E_{max}(0 \leqslant E' \leqslant E_{max}), \qquad (11)$$

where E_{max} is given by

$$E_{max} = \frac{4A}{(A + 1)^2} E_n = \Lambda E_n. \qquad (12)$$

A is the atomic weight of the primary knock-on, and E_n is the energy of the neutron (in the lab system). The average energy transferred per collision is

$$\overline{E} = \frac{1}{2} \Lambda E_n.$$

Thus if $E_{max} < L_C$, the treatment of Sec. 4.3.2. is appropriate, and the total number of atoms displaced, on the average, for each primary knock-on is

$$\nu = \overline{E}/2E_d = E_{max}/4E_d \ , \qquad E_{max} > 4E_d; \qquad (13)$$

$$\nu = 1 \ , \qquad E_{max} < 4E_d. \qquad (14)$$

If $E_{max} > L_C$, then the primary knock-on loses essentially all its energy in excess of L_C to electronic excitation, and the average number of atoms displaced for each primary knock-on (Ref. 32) is given by the relation:

$$\nu = (2 - L_C/E_{max})L_C/4E_d \ . \qquad (15)$$

Equations (13-15) form the basis for the analysis of static damage and heating.

4.3.3.1 Static damage. The total number of atoms displaced per cm^3, N_d, following neutron irradiation, is the number of primary knock-ons formed per cm^3 times the average number of displacements per primary knock-on; i.e.,

$$N_d = N_o \sigma \phi t \nu \quad , \tag{16a}$$

where N_o = atoms/cm^3 of the specimen;

σ = microscopic elastic scattering cross section of the specimen;

ϕ = neutron flux (neutrons/cm^2-sec) at the specimen;

t = time (or duration) of bombardment.

This is an overly simplified view as σ, ϕ, and ν all have dependences upon E_n, the neutron energy. In addition, ϕ may also have a time dependence; therefore, N_d is expressed correctly by

$$N_d(t) = \int_o^t \int_{E_n(t)}^{\infty} N_o \sigma(E_n') \phi(E_n', t') \nu(E_n') dE_n' \, dt' \quad , \tag{16b}$$

in which $\nu(E_n) = 1, \qquad 0 \leqslant E_n \leqslant 4E_d/\Lambda \quad ;$ (17a)

$$\nu(E_n) = \Lambda E_n/4E_d, \qquad 4E_d/\Lambda \leqslant E_n \leqslant L_C/\Lambda \quad ; \tag{17b}$$

$$\nu(E_n) = (2 - L_C/\Lambda E_n)L_C/4E_d, \qquad E_n > L_C/\Lambda \quad . \tag{17c}$$

Once again, t is the exposure time of the specimen. Note that the lower limit of integration over energy, E(t), is a function of time; this is to ensure that neutrons that have not yet arrived at the specimen are not included in the sum (integration). This arises from considerations of time of flight. If the specimen and neutron source are separated by a distance ℓ, a neutron of energy E_n takes a time $t = \sqrt{m\ell^2/2E_n}$ to travel the distance ℓ.

4.3.3.2. Heating and temperature rise. Essentially all of the energy imparted to the primary knock-on by neutron bombardment that is not expended in creating displacements is exhibited as an increase in temperature.[*] The time scales on which this happens are short enough ($\sim 10^{-11}$ s), compared to the time scale defined by the pumping process, that it is not necessary to consider the time delay between either formation of the primary knock-ons or excitation of the electrons, and relaxation of the excitation as heat. Therefore, the energy released as heat per cm^3 per second, q, is given by the relation:

$$q = N_o \sigma \phi \chi \quad , \qquad (18)$$

where χ is the average energy released as heat per primary knock-on. χ is given by

$$\chi(E_n) = \frac{1}{2}\Lambda E_n - E_d \nu(E_n) = \frac{1}{2}\Lambda E_n - E_d{}^{**} \ , \qquad 0 < E_n < 4\,\frac{E_d}{\Lambda} \ ; \qquad (19a)$$

$$= \frac{1}{4}\Lambda E_n \ , \qquad \frac{4E_d}{\Lambda} \leqslant E_n \leqslant \frac{L_c}{\Lambda} \ ; \qquad (19b)$$

$$= \frac{1}{2}\Lambda E_n - \left(2 - \frac{L_c}{\Lambda E_n}\right)\frac{L_c}{4} \ , \qquad E_n \geqslant \frac{L_c}{\Lambda} \ ; \qquad (19c)$$

where E_n, as previously defined, is the neutron energy.

---

[*] Some of the energy imparted to the primary knock-on may be lost to electrons or atoms that are knocked out of the solid, or to photons created in the solid which escape. This, however, is a very small fraction of the energy initially deposited and can be neglected.

[**] In the energy region $E_n < 4E_d/\Lambda$, Eq. (19a) indicates that χ may take on negative values. This, of course, is unrealistic. It arises from the fact that the model does not take into account the energy required to create the PKA. As this occurs only in the very low energy region, it will not affect any of the following calculations or results.

As before, the energy and time dependences should be taken into account and q written as

$$q(t) = \int_{E_n(t)}^{\infty} N_o \sigma(E_n')\phi(E_n',t)\chi(E_n')dE_n' \quad . \tag{20}$$

Once q is found, the temperature rise can be calculated by assuming a model for the heat flow. One model for heat flow is to assume a cylindrical body of radius R whose circumference is clamped at zero degrees. The equation governing this situation is

$$\frac{\partial T}{\partial t} = \frac{k}{\rho c}\nabla^2 T + \frac{q}{\rho c} \quad , \tag{21}$$

where k is the thermal conductivity of the material. If q is assumed constant, for example, at the average value $\bar{q} = \int_o^{\tau} q(t)dt/\tau$, the solution to Eq. (21) is

$$T(r,t) = \frac{\bar{q}}{4k}\{(R^2 - r^2) - 8 \sum_n e^{-\alpha\lambda_n^2 t}[R\lambda_n^3 J_1(\lambda_n R)]^{-1} J_o(\lambda_n r)\} \quad , \tag{22}$$

(see Appendix B) where $\lambda_n = (n^{th}\text{zero of } J_o)/R$; i.e., $J_o(\lambda_n R) = 0$. In this case, the centerline temperature (r = 0) is the temperature of interest. This model is not particularly realistic as any surrounding material would (probably) be heated by the neutrons to a comparable extent, thus allowing no place for the heat to relax. For this reason, this model underestimates the temperature rise.

Another model for the heat flow is to assume no heat sink. In this case, the temperature is uniform throughout a thin body and the temperature as a function of time, T(t), is given by

$$T(t) = T(t = 0) + \int_o^t \frac{\int_{E(t')}^{\infty} N_o\sigma(E_n)\phi(E_n,t')\chi(E_n)dE_n}{\rho[T(t')]c[T(t')]} dt' \quad . \tag{23}$$

Although ρ and c, the density and heat capacity, respectively, are both functions of the temperature and, therefore, time, this equation is more manageable if ρ and c are assumed constant.

4.3.3.3. Dynamic Damage. The equilibrium density of displaced recoiling atoms, D_m, is

$$D_m = N_o\sigma\phi\nu\bar{t} \quad , \tag{24}$$

in which $\bar{t}$ is defined by

$$\bar{t} = \sum_i n_i t_i/\nu \quad , \tag{25}$$

where n_i is the number of knock-ons in existence during the i^{th} generation of the cascade, and t_i is the average time the i^{th} generation lasts; i.e., the average time between the formation of the i^{th} generation of knock-ons and the formation of the $(i + 1)^{th}$ generation of knock-ons. That this formulation is correct can be seen from the following considerations: In an element of time, Δt, $N\sigma\phi\Delta t$ primary knock-ons are formed per cm^3, each of which generates ν displacements, whose average moving lifetime is $\bar{t}$. Now if $\bar{t} > \Delta t$, there will be $\bar{t}/\Delta t$ such events before the displacements formed by the first event come to rest. Thus, the contributions due to $\bar{t}/\Delta t$ events overlap, and the equilibrium density of recoiling atoms is

$$D_m = N_o \sigma\phi\Delta t\nu \frac{\bar{t}}{\Delta t} = N_o \sigma\phi\nu\bar{t} = N_o \sigma\phi\sum_i n_i t_i . \qquad (26)$$

A schematic representation of this argument is given in Fig. 6.

The reference to an equilibrium density of recoiling atoms assumes a constant neutron flux. If this is the case, D_m attains its equilibrium value (of $N\sigma\phi\nu\bar{t}$) after a time $\sim \bar{t}$ following initiation of the flux. If ϕ varies on a time scale large compared with $\bar{t}$, D_m varies similarly with time but with a lag of the order of $\bar{t}$. In Appendix A, $\bar{t}$ is estimated for materials with A = 60 and 180 by a simple model. From this estimate, $\bar{t}$ is found to be small ($\sim 10^{-12}$s). The lag of D_m relative to the flux can be neglected; thus, D_m varies as ϕ.

With this estimate of $\bar{t}$, D_m is calculated in Appendix C for A = 60 and 180, assuming a flux of 10^{25} n/cm^2-s. These calculations indicate that $\sim 10^{-8}$ of the atoms in the crystal are undergoing displacement at any time. It is, therefore, apparent that the concept of dynamic damage need be considered no further, as its effects are insignificant.

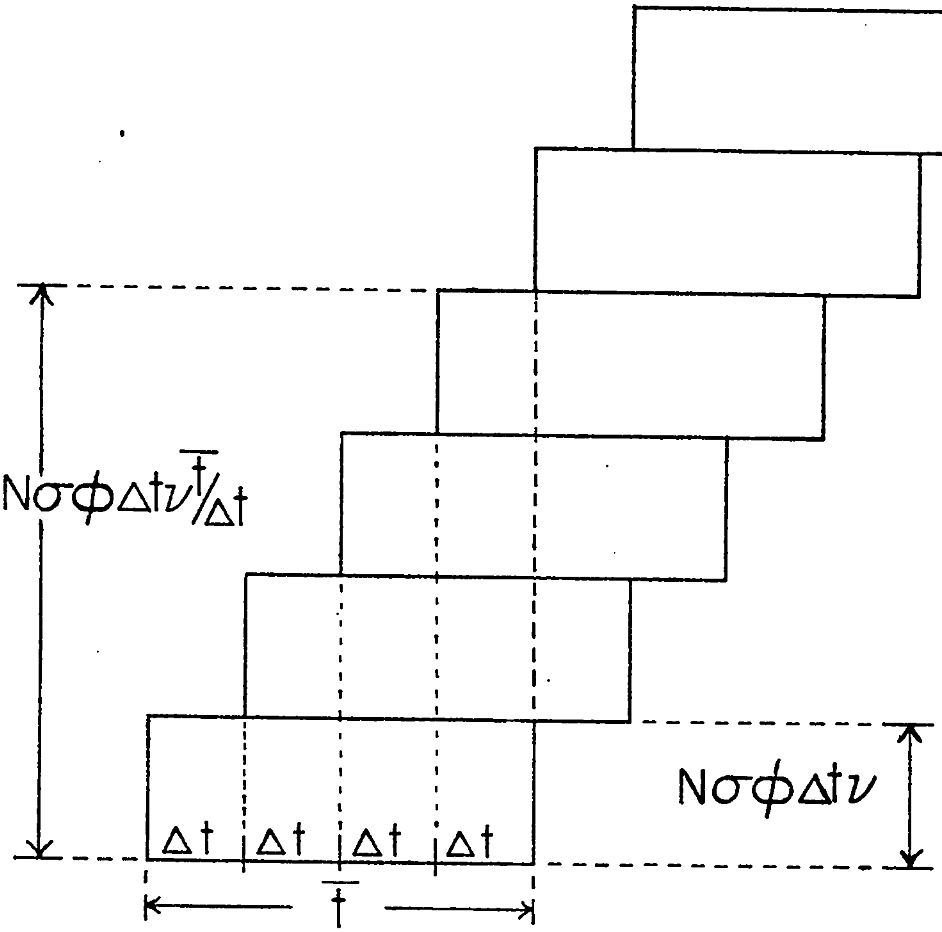

Figure 6. Schematic determination of D_m, the equilibrium density of moving atoms in a crystal during irradiation. Each of the $N\sigma\phi\Delta t$ primary knock-ons formed in the interval Δt contributes ν displacements, whose average moving lifetime is $\bar{t}$. Representing these moving atoms by a block of height $N\sigma\phi\Delta t\nu$ and of duration $\bar{t}$, it is seen that $\bar{t}/\Delta t$ such blocks always overlap. Since each block contributes $N\sigma\phi\Delta t\nu$ moving atoms and $\bar{t}/\Delta t$ blocks overlap, the equilibrium density of moving atoms is $N\sigma\phi\nu\bar{t}$.

PART 5

RADIATION DAMAGE AND THE MÖSSBAUER EFFECT

Since the Mössbauer effect is sensitive to the microscopic environments of the emitting and absorbing nuclei, microscopic changes in crystal structure affect the Mössbauer parameters. These effects may include reduction of the recoilless fraction and perturbations of the nuclear levels, resulting in isomer shifts and hyperfine interactions.

5.1. Reduction of the Recoilless Fraction

Radiation damage reduces the recoilless fraction by creating defects that introduce local vibrational modes. This increases the probability of phonon emission by exciting one of the additional modes and, thereby, reduces the recoilless fraction.

A reduction in the recoilless fraction of gold in platinum following neutron irradiation at low temperature was observed by Mansel, et al.[25] This was attributed to an increased amplitude of vibration, mainly of the Mössbauer atoms, as these are in the neighborhood of lattice defects. In other words, irradiation produces lattice defects in the neighborhood of the Mössbauer nuclei, thereby creating new local vibrational modes.

5.2. Perturbations of the Nuclear Levels

Perturbations of the nuclear levels arise from alteration of the symmetry of the crystal by radiation damage. The difference between symmetries of damaged and undamaged regions of the crystal give rise to field gradients, alteration of internal magnetic fields, and variations in the electron charge density at the nuclei of the crystal. These effects cause or alter the hyperfine interactions and isomer shifts. Variations in symmetry from point to point or region to region lead to a distribution of the values of the isomer shift and/or of the hyperfine interactions, causing the line to be broadened.

For example, Hannaford, et al.[24] used the reaction $^{118}\mathrm{Sn}(n,\gamma)^{119}\mathrm{Sn}^{m}$ to produce the Mössbauer isotope $^{119}\mathrm{Sn}^{m}$ in the inverse spinel Mg_2SnO_4. The gamma-ray cascade associated with the (n,γ) reaction imparts sufficient recoil energy to the $^{119}\mathrm{Sn}^{m}$ nucleus to cause localized damage, leading to the appearance of a secondary line in the Mössbauer spectrum at the expense of the original recoilless line. In Mg_2SnO_4, the Sn atoms are normally in an octahedrally coordinated 4^+ valence state. The secondary line is attributed to a defect configuration consisting of a divalent $^{119}\mathrm{Sn}^{m}$ ion in an octahedral site associated with a charge compensating oxygen vacancy. This, of course, causes an isomer shift. For further clarification of this experiment, see Wertheim, et al.[36]

5.3. Temperature

Heating, caused by the scattering of fast neutrons by the nuclei of the crystal, may reduce the recoilless fraction. According to the Debye model, the recoilless fraction, given by Eq. (4), decreases with increasing temperature.

5.4. Estimate of Tolerable Concentration of Defects

There is no comprehensive theory with which to estimate the alteration of the Mössbauer parameters due to radiation damage, particularly due to complex forms of damage such as displacement cascades. Simple radiation damage may be considered in terms of point defects. Gol'danskii and Kagan[10] have attempted to evaluate the line broadening due to point defects. Their results indicate that a line broadening about equal to the natural line width is reached at a relative point defect concentration of:

$$C^* \sim 10^{-6}/\tau .$$

For isomers of lifetime $\tau \sim 1$ sec., $C^* \sim 10^{-6}$; and for $\tau \sim 10^4$ sec., $C^* \sim 10^{-10}$. However, this estimate cannot be applied to short-lived isomers ($\tau \lesssim 10^{-5}$ sec.) because the implied defect concentration, C^*, is no longer low, as initially assumed in their derivation of this result. It is, therefore, necessary to look to experimental results to obtain an empirical assessment.

5.5. Observations

In this section, the results of experiments reported in the literature are reviewed in approximately chronological order. Whereas the early experiments were concerned with methods of populating Mössbauer levels and the subsequent observation of the Mössbauer effect, later experiments used the Mössbauer effect as a tool with which to study other effects; in this case, radiation damage.

1) Stone and Pillinger[37] observed the Mössbauer effect with the 59.6-keV line of ^{237}Np following both alpha decay of ^{241}Am and beta decay of ^{237}U. They observed that the recoilless fraction following beta decay was approximately a factor of 4 greater than that following alpha decay. This was attributed to local damage caused by the recoiling ^{237}Np following alpha decay of the ^{241}Am.

2) Ruby and Holland[38] observed the Mössbauer effect with the 29.4-keV line from the first excited state of ^{40}K following the ^{39}K(d,p)^{40}K reaction. No radiation damage effects were noted. The observed line breadth was attributed to the absorber thickness.

3) Hafemeister and Shera[39] used the ^{39}K(n,γ)^{40}K reaction to populate the first excited state of ^{40}K and observed the Mössbauer effect with the 29.4-keV line of ^{40}K. They concluded that the recoilless emission process is not sensitive to the method of formation of the source.

4) Seyboth, et al.[40] used Coulomb excitation to populate the 67.4-keV level of ^{61}Ni. The Mössbauer spectra so obtained showed no changes during its measurement. They observed that any radiation damage in the target seems to reach a saturation value rapidly and to remain constant for the period covered by their measurement. However, the maximum absorption of the Mössbauer spectrum was found to be only 74% of that obtained with a radioactive source. From their data, they conclude that the average Debye-Waller factor does not differ by more than 10% from that in an undisturbed nickel crystal. From these results they conclude that the Coulomb-excited nuclei in their final positions

sample a wider distribution of magnetic fields, electronic charge densities, electric field gradients, and binding energies than do nuclei in an undamaged nickel crystal.

5) Lee, et al.[41] observed the Mössbauer effect in Fe following Coulomb excitation. From the width and depth of the absorption dips they concluded that the difference in the hyperfine splittings of the source and the absorber is less than 10%.

6) Fink and Kienle[42] used the $^{155}Gd(n,\gamma)^{156}Gd$ and $^{157}Gd(n,\gamma)^{158}Gd$ reactions to populate the 89.0-keV state of ^{156}Gd and the 79.5-keV state of ^{158}Gd, respectively. They performed "mirror" experiments in which they used Gd metal as the target with Gd_2O_3 as the absorber, then Gd_2O_3 as the target with Gd metal as the absorber. The results show that the transmission line with the Gd_2O_3 target is about 10% broader than with a Gd metal target. They also observed the following relation between the recoilless fraction, f, of the targets (t) and absorbers (a) used in the "mirror" experiment:

$$\frac{f_{\text{oxide}}(t) \times f_{\text{metal}}(a)}{f_{\text{oxide}}(a) \times f_{\text{metal}}(t)} = 0.6;$$

i.e., when excitation is by an (n,γ) reaction, the recoilless fraction for an oxide lattice is only 0.6 that for a metal lattice.

7) Goldberg, et al.[43] observed the Mössbauer effect following the $^{56}Fe(d,p)^{57}Fe$ reaction. Their results are comparable to those of Lee, et al., described in #5 above.

8) Hannaford, et al.[24] studied radiation damage effects due to capture gamma recoil from the reaction $^{118}Sn(n,\gamma)^{119}Sn^m$ in the inverse spinel $^{118}SnO_2 \cdot 2MgO(Mg_2SnO_4)$. As discussed in Sec. 5.2. above, they observed a secondary line that was attributed to an isomer shift caused by the defect configuration.

9) Czjzek, et al.[44] observed the Mössbauer effect with the 67.0-keV line of ^{73}Ge following Coulomb excitation. The width of the emission spectrum of the target was consistent with the natural width. No comparison with unirradiated data was possible, as this was the first observation of the 67.0-keV line by Mössbauer techniques.

10) Ritter, et al.[45] used Coulomb excitation of ^{57}Fe to observe the Mössbauer effect in α-iron and in Fe_2O_3. Within experimental error, the Mössbauer fraction following Coulomb excitation in α-iron is not less than that observed with ^{57}Co sources; whereas, in the case of the oxide, a reduction of the recoilless fraction by a factor of 2 is observed. In both the metallic and the oxide data, the respective hyperfine splittings do not deviate by more than a few percent from the values obtained with ^{57}Co sources for α-iron and for Fe_2O_3, respectively. However, an absorption line at -6.33 mm/sec does appear in the Fe_2O_3 data. It was speculated that this line arises from recoilless emission from sites other than normal iron sites in an Fe_2O_3 lattice. There is no indication in any of the Coulomb excitation data of isomer shifts differing from the shifts observed with ^{57}Co sources. These results were interpreted in terms of extensive replacement collisions.

11) Czjzek, et al.[46] used recoil implantation techniques to implant Coulomb-excited ^{73}Ge into a chromium host. They observed no changes in the Mössbauer spectrum during an irradiation time of approximately one week. They also observed the Mössbauer effect for ^{73}Ge in germanium by use of a germanium target. The recoilless fraction of this target was very small compared to that of a germanium absorber. An X-ray investigation of the targets before and after irradiation showed complete conversion from the crystalline to an amorphous state. They also observed that the recoilless fraction of GeO_2 tetragonal is approximately five times greater than the recoilless fraction of GeO_2 hexagonal.

12) Berger, Fink and Obenshain[47] observed the Mössbauer effect in metallic iron, Fe_2O_3, and in $FeSO_4 \cdot 7H_2O$ following the $^{56}Fe(n,\gamma)^{57}Fe$ reaction. They compared these spectra with those of nonirradiated samples. For metallic iron, they observed no alteration of the Mössbauer parameters and concluded that, either the recoil nuclei are in normal lattice positions, or that a vacancy has a very small effect on the hyperfine interaction at an adjacent iron nucleus. For the Fe_2O_3 target, they observed a 4% decrease in the separation of the outer lines for the irradiated sample as compared with the unirradiated sample. They observed that this decrease of the effective magnetic field could be explained by the assumption that not all atoms come to rest at a lattice site with the normal valence of the iron ions. With the $FeSO_4 \cdot 7H_2O$ they observed an asymmetry in the spectrum that suggested that it was the superposition of two spectra. A mixture of 0.6 Fe^{2+} + 0.4 Fe^{3+} gave a reasonable fit.

13) Zimmermann, et al.[48] used Coulomb excitation of ^{73}Ge to observe the Mössbauer effect in crystalline Ge, Ge-Cr alloy, GeO_2 (hexagonal), and GeO_2 (tetragonal) absorbers. They observed that the crystalline germanium target was converted to the amorphous state by the ion bombardment. It was also observed that the Debye temperatures of the Ge-Cr alloy and the Ge-implanted Cr target are equal, indicating that radiation damage was insignificant for the implantation target. The observed line widths were 1.01, 1.26, 0.98, and 1.44 of the natural linewidth for the Ge (crystalline), Ge-Cr (alloy), GeO_2 (tetragonal), and GeO_2 (hexagonal) absorbers, respectively. It was also noted that the recoilless fraction of GeO_2 (tetragonal) is greater by a factor of 6 than the recoilless fraction of GeO_2 (hexagonal).

14) Hardy, et al.[49] observed the Mössbauer effect with ^{183}W following Coulomb excitation. The recoilless fraction of the target was smaller than the theoretical value. This was attributed to the excited nuclei's coming to rest at abnormal lattice positions or to local heating.

15) Jacobs, et al.[50] observed the Mössbauer effect in HfC, HfN, HfB_2, HfO_2, and Hf metal following Coulomb excitation of ^{177}Hf, ^{178}Hf, and ^{180}Hf. They observed that the recoilless fractions and the details of the Mössbauer spectra remain unchanged during the course of the experiment. Also, Debye-Scherrer X-ray powder patterns of the HfC and HfN targets were consistent with stoichiometric composition and showed no changes after irradiation. The observed line widths were 2.58 ± 0.2, 2.09 ± 0.17, 2.42 ± 0.25, 2.67 ± 0.31, and 1.97 ± 0.24 of the natural linewidth, in the

case of HfC, HfN, HfO_2, HfB_2, and Hf metal, respectively. These increased linewidths were attributed to anomalous hyperfine interactions, which were interpreted in terms of lattice distortions resulting from vacancies produced in the locality of the decaying recoil Mössbauer nucleus following Coulomb excitation. The degree of lattice distortion was found to be dependent upon the bonding characteristics of the compounds.

16) Barros, et al.[51] implanted ^{57}Co directly into a diamond single crystal and observed the Mössbauer spectrum following decay to ^{57}Fe. They observed a two-line spectrum, which was attributed to quadrupole splitting. The quadrupole splitting occurs because the Fe interstitial in the diamond lattice does not reside exactly in a position of tetrahedral symmetry. The openness of the diamond lattice, which makes the off-center displacements possible, also allows the iron interstitials to have increased amplitudes of vibration. This accounts for the small recoilless fraction observed.

17) Mansel, et al.[25] measured the Debye-Waller factor of gold in platinum after low-temperature irradiation with neutrons. This was found to affect the Debye-Waller factor but none of the other Mössbauer parameters. They used $^{196}Pt(n,\gamma)^{197}Pt \xrightarrow[\beta^-]{20\ hr} {}^{197}Au$ reactions to introduce the Mössbauer isotope ^{197}Au into the platinum samples. Exposure to fast neutrons alone produced no measurable decrease of the Debye-Waller factor (the ^{197}Pt is formed during a pre-irradiation, during which the correlated damage is annealed out.) Exposure to thermal neutrons alone reduces the recoilless fraction by approximately 4%.

Exposure to a combined flux causes the recoilless fraction to change from 0.96 f_o (for zero fast neutron dose) to approximately 0.90 f_o when the fast neutron dose is increased. Nearly total saturation of the reduction effects seems to occur already at doses ϕt (E > 0.1 MeV) = 3×10^{17} n/cm^2. At this dose, the residual electrical resistivity of platinum and, therefore, the mean concentration of defects produced by fast neutrons (bulk damage), still increases linearly with dose. From these observations they conclude that the reduction of the Debye-Waller factor is not caused by a change of the vibrational behavior of the whole lattice, but is caused by a higher vibration amplitude mainly of the Mössbauer atoms as these are in the neighborhood of lattice defects.

18) Mekshes and Hershkowitz[52] used Coulomb excitation to populate the first excited levels of ^{182}W, ^{184}W, and ^{186}W, in tungsten metal targets. They observed that line broadening may be minimized by use of cubic non-magnetic metal targets. They concluded that the natural linewidths of ^{182}W, ^{184}W, and ^{186}W are 1.994 mm/sec, 1.92 mm/sec, and 1.62 mm/sec, respectively; whereas the observed linewidths, before correcting for quadrupole interactions, are 2.54 mm/sec, 2.35 mm/sec, and 1.994 mm/sec for ^{182}W, ^{184}W, and ^{186}W, respectively. This broadening was attributed to an electric quadrupole interaction arising from the source nuclei's being in abnormal environments.

It was also observed that, although the recoilless fractions of the source nuclei could not be accurately determined, the mean value was lower than the corresponding values of recoilless fractions of the absorber nuclei. This was attributed to a temperature difference between source and absorber.[53]

19) Hardy, et al.[54] observed reduced recoilless fractions following Coulomb excitation for the short-lived isomers: ^{165}Ho (97 keV, $t_{1/2} \approx 20$ ps), ^{167}Er (79 keV, $t_{1/2} \approx 100$ ps), and ^{175}Lu(113 keV, $t_{1/2} \approx$ 100 ps). They observed no Mössbauer effect for the shortest-lived isomer (^{165}Ho) and a reduced effect for the longer-lived isomers ($t_{1/2} \approx 100$ ps). This was attributed to thermal spikes. They calculate that, at a time 20 ps after the ion comes to rest in a rare earth oxide, $\Delta T = 200°$ K, and that this accounts for the absence of a Coulomb-excitation Mössbauer effect. For times of the order of 10^{-9} sec, the model predicts $\Delta T < 1°$ K, which would be expected to cause no measurable decrease in the Mössbauer effect for longer-lived states.

20) Wender and Hershkowitz[55] simultaneously measured the recoilless fractions, following Coulomb excitation, of the 185-ps (46.5-keV) ^{183}W and 1.37-ns (100.1-keV) ^{182}W states. Their results could not be explained in terms of thermal spikes as suggested by Hardy, et al.[19] The results were consistent with recoilless emission from different sites with different mean square displacements. Their observations suggest that 0.6 of the nuclei decay from sites from which emission is substantially reduced. A possible explanation is given in terms of local amorphization.

21) Lambe and Schroeer[56] observed radiation-induced isomer shifts in a Eu_2O_3 target following Coulomb excitation of the 21.6-keV state of ^{151}Eu. At 85° K, the linewidth is more than twice that observed at room temperature. This is attributed to electronic perturbations.

22) Vogl, et al.[26] have studied radiation damage in α-iron, doped with 0.6 atomic per cent Os. They used the reactions $^{192}\text{Os}(n,\gamma)^{193}\text{Os} \xrightarrow[\beta]{31\text{ h}} {}^{193}\text{Ir}$ to populate the 73.1-keV state of ^{193}Os. The capture gamma-ray recoil causes the ^{193}Os to reside in the neighborhood of a defect (correlated damage). The local environment of the ^{193}Os nuclei was inferred from the Mössbauer spectrum of the ^{193}Ir. Significant differences of the Mössbauer magnetic hyperfine field and of the linewidth between the irradiated and fully annealed samples were observed. Their results indicate that there is no dependence of the Mössbauer parameter changes on irradiation dose. A fit of the Mössbauer spectrum of the irradiated sample with two eight-line spectra suggests that 40% of the Mössbauer Ir atoms reside in radiation-modified lattice locations, with a 6% reduction in the local magnetic field. They conclude that these modified lattice locations have a vacancy in their nearest neighbor shell. To further demonstrate that these effects arise from correlated damage, they irradiated an α-iron sample with approximately 5.2×10^{18} fast n/cm^2; this was then used as a ^{57}Fe Mössbauer absorber. This experiment showed no irradiation-produced changes in the Mössbauer hyperfine parameters.

23) Wender and Hershkowitz[57] studied the short-time effects of irradiation upon WC, WB, W_2B, W_2B_5, WO_3, and WS_2 by observing the Mössbauer effect of tungsten nuclei following Coulomb excitation. Values for the recoilless fraction, hyperfine interaction, and linewidth were determined in the nonirradiated materials using a tungsten metal target with tungsten compound absorbers. These parameters were compared with those obtained by

observing the Mössbauer effect using tungsten-compound targets and tungsten-metal absorbers. They assumed, on the basis of Ref. 52, that the recoilless fraction of tungsten metal is not changed by irradiation.[53] Anomalous hyperfine interactions were observed in all irradiated compounds. The recoilless fraction was found to be reduced in most of the materials. In WO_3 it was found that the fractional reduction in recoilless fraction does not depend on the gamma-ray energy and is time independent. This was attributed to the formation of local amorphous regions. A partial summary of their results is shown in Table V.

5.6. Summary of Relevant Observations

Reductions of the recoilless fraction have been observed following alpha decay, Coulomb excitation, and neutron excitation. The magnitude of the reduction, indeed, the magnitudes of all the effects depend on the material in which the Mössbauer effect is being observed. Since the graser will probably require neutron excitation and the properties of concern are affected by neutron irradiation, it is desirable to study the effects of neutron excitation and irradiation upon the Mössbauer effect. However, it may be concluded from the observations (Sec. 5.5, #17, 22) that it is correlated damage that is responsible for the alterations of the Mössbauer parameters and that uncorrelated fast neutron damage alone does not produce significant changes in the Mössbauer spectrum. In fact, the maximum reduction occurs when correlated damage is accompanied by bulk damage, which acts as a diffusion activation mechanism (see Sec. 5.5, #17). Coulomb excitation (as well as any other

TABLE V[a]

COMPARISON OF VALUES FOR f AND Γ IN IRRADIATED VERSUS NONIRRADIATED MATERIALS

Material	Mössbauer Isotope	E_γ	$\Gamma_n{}^{b}$	Nonirradiated		Irradiated	
				$f_o{}^{c}$	$\Gamma_o{}^{bc}$	f'^{d}	Γ'^{bd}
W metal	^{182}W	100.1	.997	.186	NA	.186	2.04
	^{184}W	111.2	.96	.13	NA	.13	2.0
	^{186}W	122.6	.805	.088	NA	.088	2.02
	^{183}W	46.48	17.6	.77	NA	.77	19.2
WC	^{182}W			.22	1.16	.132	2.58
	^{184}W	(")	(")	.16	1.00	.08	2.16
	^{186}W			.13	0.90	.056	2.76
	^{183}W			.72	--	.55	--
WB	^{182}W			.10	1.30	.187	2.34
	^{184}W			.06	0.92	.10	2.70
	^{186}W			--	--	.062	2.14
W_2B	^{182}W			.20	1.06	.094	1.72
	^{184}W	(")	(")	.14	1.12	.049	2.02
	^{186}W			.10	1.04	.069	7.84
W_2B_5	^{182}W			.25	1.04	.22	3.02
	^{184}W	(")	(")	.20	0.76	.079	3.30
	^{186}W			.13	1.14	.025	--
WO_3	^{182}W			.075	1.28	.025	3.26
	^{184}W	(")	(")	.039	0.96	--	--
	^{186}W			.016	0.46	--	--
	^{183}W			.57	--	.29	--
WS_2	^{182}W			.06	1.94	--	--
	^{184}W	(")	(")	.04	1.64	--	--
	^{186}W			.03	1.76	--	--

---

a) Adapted from Ref. 57.
b) All linewidths expressed by FWHM in mm/s.
c) The subscript o refers to the nonirradiated values.
d) The superscript ' refers to the irradiated values.

excitation-damage mechanism) experiments provide excellent data from which to assess the effects of correlated damage upon the Mössbauer parameters.

From Coulomb excitation as well as neutron bombardment experiments, it may be concluded that bulk damage is not responsible for significant alteration of the Mössbauer parameters. This is supported by the observation (Sec. 5.5., #4,11,15) that the Mössbauer spectrum does not change during the course of the experiment. Therefore, for the purposes of this thesis, the effects of radiation damage should be assessed from data obtained from correlated damage experiments. An overview of these experiments indicates that the particular effects of radiation damage on the Mössbauer parameters are determined predominantly by properties of the particular materials.

In general, the recoilless fractions of cubic metal targets are affected least by irradiation. Where comparisons are possible in the preceding observations, with but one exception (WB) it is found that there is less reduction of the recoilless fraction in metal targets than in compounds.

A property of several materials, which affects the recoilless fraction following irradiation, is the tendency to amorphize under irradiation (see Sec. 5.5, #11, 13, and 23, also Ref. 27). In this case the recoilless fraction is reduced significantly. The model of Kelly and Naguib[27] (discussed in Sec. 4.2.1.) may be used to predict this behavior in non-metallic compounds. Pure monatomic metals do not amorphize under irradiation.

Increased linewidth due to irradiation is also minimized by the use of nonmagnetic metal targets (see Sec. 5.5, #15, and 18) with nonmagnetic cubic metal targets being affected least (#18). This is explained by the facts that nonmagnetic, cubic materials in an undamaged state have no hyperfine splittings to cause broadening and that, when irradiated, these metals tend to undergo replacement collisions. Computer simulations of radiation damage[30,31] indicate that the probability for replacement collisions is high in a cubic lattice. Thus, for a correlated damage-excitation reaction, such as Coulomb excitation or the (n,γ) reaction, the excited nucleus generally ends up on a normal lattice site with a nearby vacancy (see Sec. 5.5, #22). Variations in the defect configurations may then cause line broadening.

A polyatomic lattice presents a greater probability for alteration of local symmetry and chemical effects. Not only is the probability for replacement collisions less than in a metal, but it is likely that in a compound collisions may create additional asymmetries not found in a monatomic lattice. In an ordered compound, replacement collisions lead not only to defect configurations similar to those of a monatomic lattice, but also to additional asymmetries involving the interchange and displacements of different atomic species. This is believed to account for increased linewidth and additional lines observed for compounds.

Another property that determines linebreadth in an irradiated compound is bond character. Increases of linewidth following Coulomb excitation have been attributed to anomalous hyperfine interactions caused by lattice distortions (see Sec. 5.5, #15). The degree of lattice distortion is dependent upon the bending characteristics of the compounds.

Other properties of materials affecting the Mössbauer parameters are the Debye temperature, the openness of the lattice, the lattice type, and the coordination number of the Mössbauer nucleus. The Debye temperature determines the recoilless fraction according to Eq. (4). The openness of the lattice affects both the recoilless fraction and the hyperfine splitting of Mössbauer nuclei in interstitial positions. This was demonstrated by Barros, et al.[51] who ion implanted ^{57}Co in diamond. The large interstitial volume in which the ^{57}Co nucleus resides allows a large $\langle x^2 \rangle$ and, therefore, a reduced recoilless fraction. It also allows the implanted nucleus to reside off center, so that the asymmetry causes quadrupole splitting of the line.

The lattice type and coordination number of the Mössbauer nucleus are interrelated. They may affect both the recoilless fraction and the linebreadth. Gol'danskii, et al. are reported[48] to have observed an increasing recoilless fraction with increasing coordination numbers of Sn compounds. It has also been observed[46,48] (see Sec. 5.5, #11, and 13) that the recoilless fraction of tetragonal GeO_2 is at least five times greater than the recoilless fraction of hexagonal GeO_2. This has been attributed[48] to the tetragonal form's having a higher coordination number than the hexagonal form. The hexagonal form also exhibits a broader line than the tetragonal form. This is believed to be caused by weak quadrupole splitting in the hexagonal form.

5.7. Unanswered Questions

In the preceding sections it has been assumed that bulk damage may be ignored. Certainly experimental evidence supports this view. Mansel[25] and Vogl[26] have demonstrated that the changes in the Mössbauer parameters caused by neutron irradiation (at least in pure metals) are due only to correlated damage. Mansel[25] has also shown that additional alteration of the Mössbauer parameters caused by fast neutrons is observed only in conjunction with correlated damage, and that this effect saturates at the relatively low dose of $\sim 3 \times 10^{17}$ n/cm^2. At this dose the electrical resistivity, which is a measure of bulk damage, is still increasing linearly with dose, indicating that bulk damage is nowhere near to saturation. It seems only reasonable to assume that at some point the effects of bulk damage upon the Mössbauer parameters should become evident. The question is: At what point do they become evident?

Figure 7 is an adaptation and extrapolation of the results of Mansel et al.[25] The point labeled 1 is an interpolation based upon the observation of Vogl et al.[26] that there is no change in the hyperfine parameters following a fast neutron dose of $\sim 5 \times 10^{18}$ n/cm^2. Using Eq. (15) (see Appendix D), this corresponds to a displacement concentration of $\sim$ 1%. It is, therefore, reasonable to assume that bulk damage effects may be neglected at displacement concentrations below 1%, as characterized by the model developed in Sec. 4.3.

As the displacement concentration increases still further, the curve passes through a transition region (region II) and into region III--

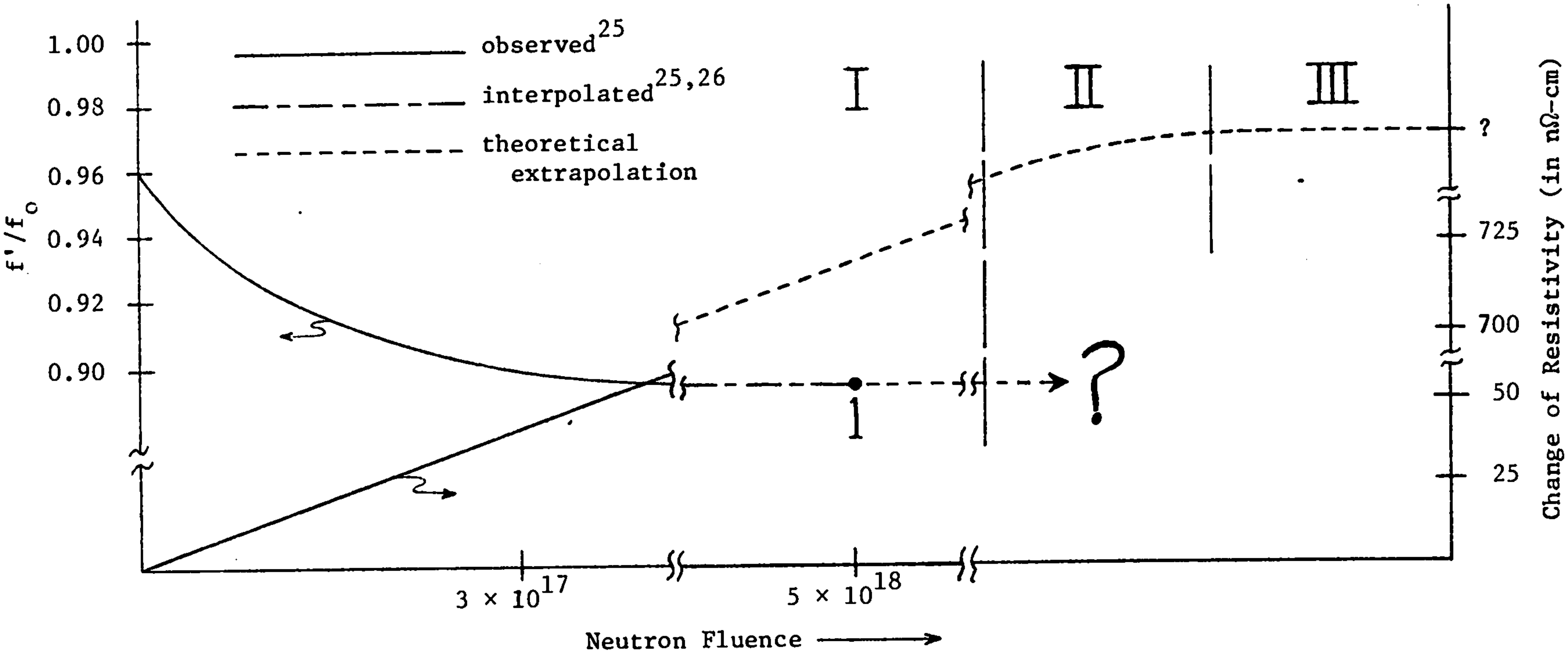

Figure 7. The effect of fast neutron irradiation in conjunction with correlated damage upon the recoilless fraction and electrical resistivity. The electrical resistivity increases linearly with fluence (Region I), breaks away from linearity and approaches a constant value (Region II), and finally remains constant (Region III). The solid lines are based on the results of Mansel et al.[25] who observed that the electrical resistivity increased linearly while the recoilless fraction of a sample irradiated by thermal neutrons (causing correlated damage) diminished from 0.96 of that for an annealed sample to $\sim$ 0.90 as the fast neutron dose was increased from 0.0 to 5.5×10^{17} fast-n/cm^2. The broken line is an interpolation between the results of Mansel et al.[25] and those of Vogl et al.,[26] shown by the point labeled 1. The dashed lines are theoretical extrapolations. In Regions II and III the electrical resistivity breaks away from a linear dependence on the fluence and approaches some constant value; it is unknown what happens to the recoilless fraction in these regions.

the saturation region. In this region the bulk damage has saturated, as indicated by the constancy of the electrical resistivity curve. The values of the recoilless fraction (and linebreadth) in regions II and III cannot be predicted on the basis of their behavior in region I. However, the graser should operate in region I, as will be shown in Section 6. Thus, the behavior of the recoilless fraction (or linebreadth) in regions II and III need not be considered to adequately assess radiation damage effects in a graser.

PART 6

RADIATION DAMAGE AND THE GRASER PROBLEM

6.1. Temporal Considerations and Reduction Factors

The graser application of the Mössbauer effect differs greatly in time scale from use of the conventional Mössbauer effect as a probe. The damage accumulates and the resonance is observed much more rapidly in the graser application. In a Mössbauer experiment, the damaging radiation is delivered over an extended period and the resonance absorption events are observed over a period of many hours while the spectrum accumulates. In a burst-pumped graser, resonance emission can be observed for only an interval, a few times the natural lifetime, in which the photon avalanche develops. The pumping must take place in a time short compared to the natural lifetime. Therefore, the radiation damage that occurs due to the pumping also accumulates in an interval short compared to the natural lifetime.* Thus, if one wishes to predict radiation damage effects upon the Mössbauer spectrum, which were discussed in Sec. 5, one must identify and analyze differences associated with the different time scales; namely, time dependence of σ_{se} and of the temperature rise associated with pumping.

---

*Actually, the neutron flux required for pumping will be present not only during the initial pumping to inversion, but throughout the lasing process, as it is not possible to generate a narrow pulse under the conditions anticipated. Therefore, damage will accumulate throughout the lasing process.

6.1.1. Radiation Damage and Reduction of the Resonance Cross Section

It has been established in Sec. 5.1. that radiation damage may alter the recoilless fraction, f, and the observed linewidth, Γ, and that σ_a depends on f/Γ. In addition, the time dependence of σ_{se} is determined by Γ; the larger Γ, the faster σ_{se} attains its asymptotic value. The problem that must therefore be addressed is: How does σ_{se} vary with time while the graser body is subjected to damaging radiation?

Figure 8 is a qualitative representation of σ_{se} as a function of time. Figure 8(a) represents the case in which $1/\Gamma = 1/\Gamma_o$, where Γ_o is for the undamaged crystal. In case (b), $1/\Gamma = 1/(2\Gamma_o)$. Notice that the asymptotic value of σ_{se} is 1/2 of that in case (a), but that it takes less time to attain this value. Figure 8 is drawn such that the time required to attain a given fraction of σ_a [$= (f/\Gamma)\sigma_{ao}$] varies as $1/\Gamma$; i.e., the time it takes σ_{se} to attain a given fraction of σ_a is twice as long for the case where $1/\Gamma = 1/\Gamma_o$ as it is for the case in which $1/\Gamma = 1/(2\Gamma_o)$. Although the actual time dependence may not vary with Γ precisely in this manner, it is satisfactory to assume so for illustrative purposes. To attempt to deal with the exact time dependence of the development of σ_{se} adds unnecessary complication; it can be shown that the problem may be treated satisfactorily without such considerations.

Figure 8(c) represents the case in which $1/\Gamma$ is slowly decreasing during the development of σ_{se}. Notice that $1/\Gamma$ does not decrease appreciably during the time it takes σ_{se} to develop to its asymptotic value, so that the time dependence does not differ greatly from that of case (a).

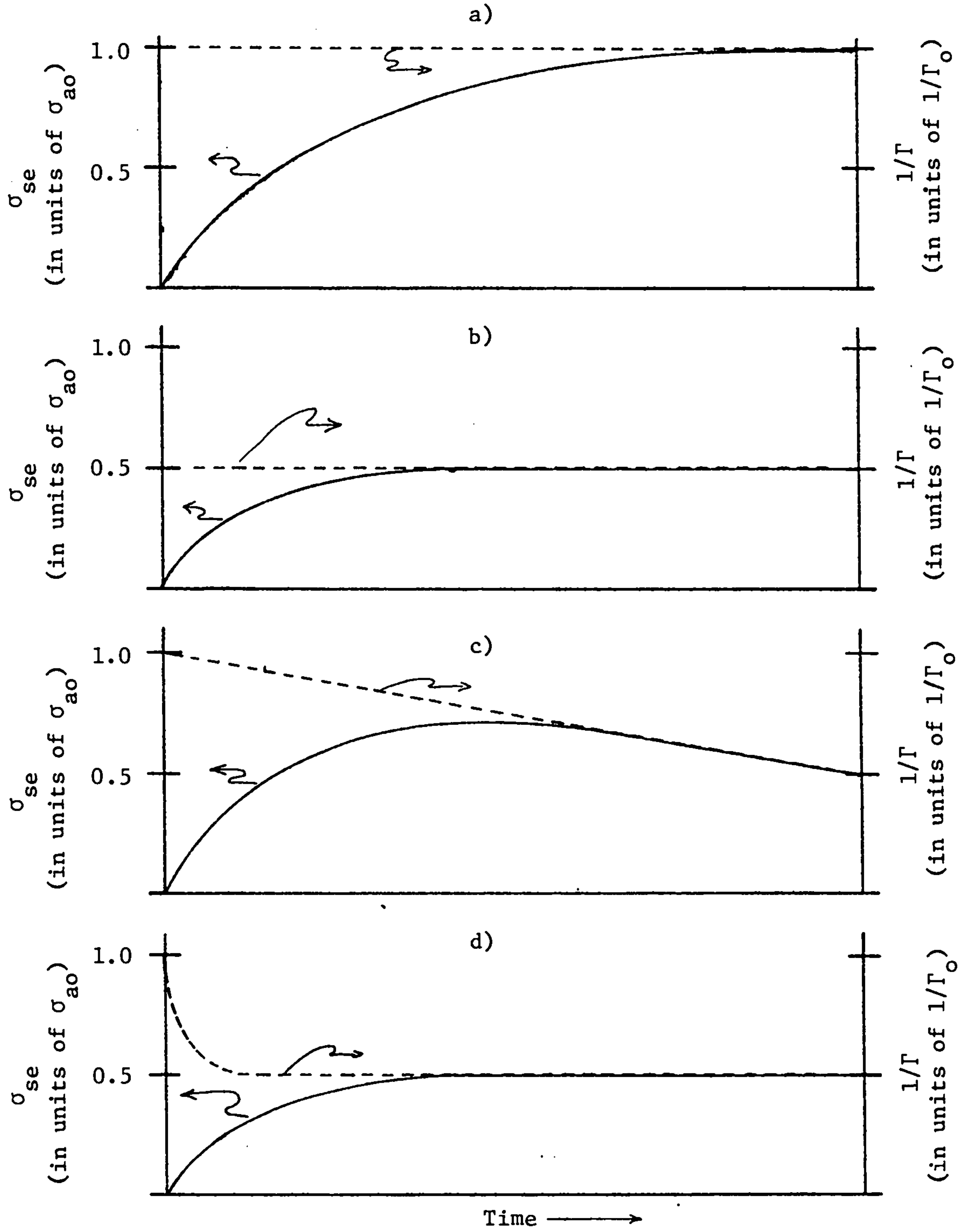

Figure 8. A qualitative representation of σ_{se} as a function of time:
a) $1/\Gamma = 1/\Gamma_o$,
b) $1/\Gamma = 1/(2\Gamma_o)$,
c) $1/\Gamma$ decreasing slowly from its initial value of $1/\Gamma_o$,
d) $1/\Gamma$ decreasing very rapidly from $1/\Gamma_o$ to $1/(2\Gamma_o)$.

Figure 8(d) represents the case in which $1/\Gamma$ decreases very rapidly to $1/(2\Gamma_o)$. The time dependence in this case is virtually identical to that of case (b).

It may be argued that, when the (n,γ) reaction is the excitation mechanism, the capture-γ recoil, which is responsible for the correlated damage, precedes formation of the isomer of interest; and, therefore, the damage that is responsible for line broadening is present from the moment the isomer of interest is formed. This situation is represented by Fig. 8(b). This argument is particularly suited to those monatomic metals in which, as seen in Section 5, line broadening due to bulk damage effects is minimal.

In cases where bulk damage effects are also significant (e.g., as the DPA approaches one) the correlated damage causes an immediate increase of the linebreadth to a value that afterward remains constant in time, while bulk damage causes the linebreadth to continue to increase. If the neutron pulse is very short compared with τ, then the linebreadth will increase very rapidly, in a manner similar to that represented in Fig. 9. This behavior is similar to that in Fig. 8(d), and may be approximated by Fig. 8(b). If the fast neutrons, which are responsible for bulk damage, precede those that are captured, so that the bulk damage precedes the capture process, then both forms of damage precede formation of the isomer of interest. This situation is similar to that represented in Fig. 8(b). Thus, if all the damage occurs before or very shortly after formation of the isomer of interest, the time dependence of the development

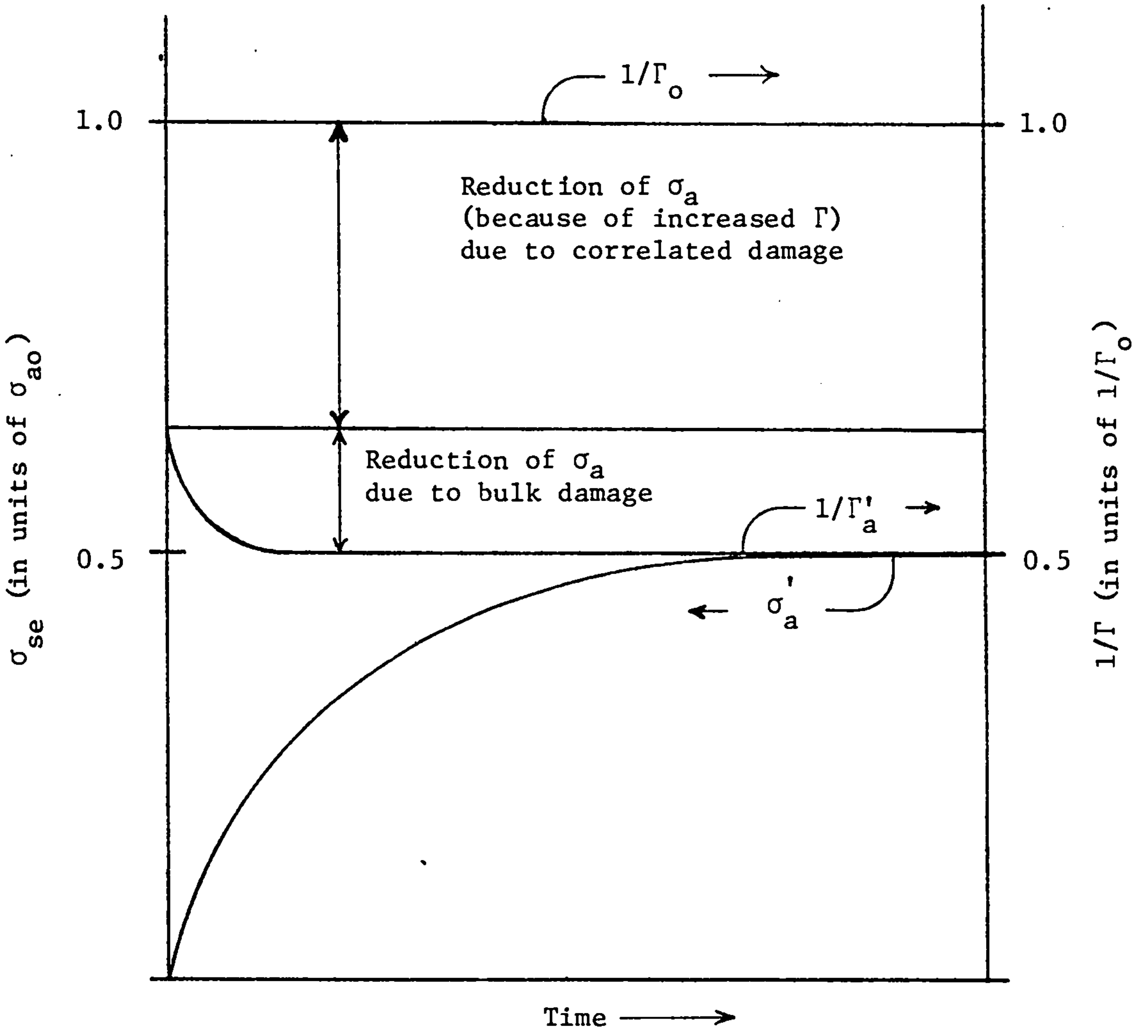

Figure 9. A qualitative representation of σ_{se} as a function of time for the case in which both correlated and bulk damage contribute to the linebreadth.

of σ_{se} is governed by the asymptotic value of the linebreadth in the damaged crystal, Γ'_a, and may therefore be represented by Fig. 8(b).

If, however, the neutron pulse is broad relative to τ, then the linebreadth may change during the development of σ_{se}. The exact variation of Γ with time has not yet been determined. A conservative approach to this problem is to assume that the time dependence of the development of σ_{se} is determined by Γ_o while the amplitude is determined by Γ'_a. This is equivalent to designing for the worst possible circumstances, as conditions for lasing are more stringent the slower σ_{se} develops and the smaller its final amplitude. The time dependent cross section may then be given by

$$\sigma'_{se}(t) = R_\Gamma \, \sigma_{se} \, (t, \Gamma = \Gamma_o) \ , \tag{27}$$

where the reduction factor, R_Γ, is defined by

$$R_\Gamma \equiv \Gamma_o / \Gamma'_a \ . \tag{28}$$

Similar arguments hold for f, the recoilless fraction.

If all the damage occurs before or very shortly after formation of the isomer of interest, then the asymptotic value of f in the damaged crystal, f'_a, may be substituted for f in Eq. (2). If, however, the neutron pulse is broad relative to τ, f varies with time, introducing an additional, separable time dependence into σ_{se}. The exact time dependence of f is extremely difficult, if not impossible, to determine; however, as before, the conservative approach is to consider the worst possible case, which is to let $f = f'_a$.

Introducing another reduction factor,

$$R_f \equiv f'_a/f_o \quad , \tag{29}$$

the time dependent cross section may now be written as

$$\sigma'_{se}(t) = R_f R_\Gamma \sigma_{se}(t, \Gamma = \Gamma_o, f = f_o).$$

The importance of these reduction factors is that they are easily measured by conventional Mössbauer experiments. Since the latter measure asymptotic values of f and Γ, comparison of measurements of f and Γ in irradiated versus nonirradiated crystals yields the reduction factors R_f and R_Γ. In many cases these data are available in the literature, as summarized in Sec. 5. This approach has the additional advantage that it leads to the most conservative estimates of $\sigma_{se}(t)$; this is preferable for a feasibility study.

6.1.2. Temperature Rise and Associated Reduction of the Resonance Cross Section

The population inversion for the graser demands an extremely intense neutron flux. If this is supplied by a nuclear explosion, the surrounding environment is also subjected to as intense a neutron flux. Therefore, both the graser crystal and its surroundings are heated by neutron scattering, and there can be no heat sink to maintain the temperature of the graser crystal. As the temperature of the graser crystal increases, the recoilless fraction changes, introducing yet another time dependence into σ_{se}. Since the recoilless fraction enters only into the amplitude of σ_{se}, this time dependence is also separable and may be treated as a time-dependent reduction factor. Therefore,

$$\sigma'_{se}(t) = R_T(t)R_f R_\Gamma \sigma_{se}(t, \Gamma = \Gamma_o, f = f_o) \quad , \tag{30}$$

where

$$R_T(t) \equiv f[T(t)]/f_o . \tag{31}$$

The temperature dependence of the recoilless fraction should be measured by experiment, because anomalous temperature effects have been observed.[58] However, as a first approximation the Debye model is adequate. In this case the recoilless fraction is given by Eq. (4) and $f_o = f(T_o)$. The temperature as a function of time is given by Eq. (23). Thus all quantities required to evalute $\sigma_{se}(t)$ are now available.

6.2. Evaluation of the Reduction Factors

Provided there is no annealing during delivery of the dose, the damage accompanying the total neutron dose should not depend on the delivery time. The reduction factors that have been defined in terms of properties observed following long term irradiation should therefore be the same for the graser application, since annealing is prevented in long term irradiations by use of cryogenic temperatures. The reduction factors as determined from long term irradiation data are listed in Table VI. As discussed in Sec. 5.7, these results are appropriate in cases where the concentration of displacements is less than 1%.

TABLE VI

EVALUATION OF R_f AND R_Γ FROM DATA OBTAINED FROM IRRADIATED VERSUS NONIRRADIATED MATERIALS

Ref.	Isotope/Material	Radiation	Γ_n	Γ_o	f_o	Γ'	f'	$R_f = \frac{f'}{f_o}$	$R_\Gamma = \frac{\Gamma_o}{\Gamma'}$
[25]	$^{197}Au/Pt$	thermal ^1_0n	5.5	--	a	6.5	.96 f_o	.96	.85 [b]
		fast ^1_0n	5.5	--	a	6.5	1.0 f_o	1.00	.85 [b]
		thermal+fast	5.5	--	a	6.5	.90 f_o	.90	.85 [b]
[26]	$^{193}Ir/Fe$	thermal+fast		∿.91	---	1.28	---	---	.71
[57]	$^{182}W/W$	6 MeV $^4He^+$	.997	--	.186 [c]	2.04	.186	1.0	.49 [b]
	$^{184}W/W$	6 MeV $^4He^+$	.96	--	.13 [c]	2.0	.13	1.0	.48 [b]
	$^{186}W/W$	6 MeV $^4He^+$	.805	--	.088 [c]	2.02	.088	1.0	.40 [b]
[57]	$^{182}W/WC$	6 MeV $^4He^+$	(")	1.16	.22	2.58	.132	.60	.45
	$^{184}W/WC$	6 MeV $^4He^+$		1.0	.16	2.16	.08	.50	.46
	$^{186}W/WC$	6 MeV $^4He^+$		0.90	.13	2.76	.056	.43	.33
[57]	$^{182}W/WB$	6 MeV $^4He^+$	(")	1.30	.10	2.34	.187	1.87	.56
	$^{184}W/WB$	6 MeV $^4He^+$		0.92	.06	2.70	.10	1.67	.34
[57]	$^{182}W/W_2B$	6 MeV $^4He^+$	(")	1.06	.20	1.72	.094	.47	.62
	$^{184}W/W_2B$	6 MeV $^4He^+$		1.12	.14	2.02	.049	.35	.55
	$^{186}W/W_2B$	6 MeV $^4He^+$		1.04	.10	7.84	.069	.69	.13
[57]	$^{182}W/W_2B_5$	6 MeV $^4He^+$	(")	1.04	.25	3.02	.22	.88	.34
	$^{184}W/W_2B_5$	6 MeV $^4He^+$		0.76	.20	3.30	.079	.40	.23
[57]	$^{182}W/WO_3$	6 MeV $^4He^+$	(")	1.28	.075	3.26	.025	.33	.39

---

a) A numerical value was not given for f_o; f' was expressed as a fraction of f_o.
b) This value based on the natural width; i.e., $R_\Gamma = \Gamma_n/\Gamma'$.
c) Based upon earlier work [52], it was assumed that $f_o = f'$.

6.3. Evaluation of the Maximum Allowable Temperature Rise

The requirement for gamma-ray amplification by stimulated emission, given by relation (1a), may be rewritten as

$$N^{*}\sigma'_{a} > N\sigma_{NRA} \quad . \tag{32}$$

where σ'_a has been substituted for σ_a to account for the pumping and consequent radiation damage; therefore, the inequality may be written as

$$N^{*}\sigma'_{a} = N^{*}R_{T}(t)\ R_{f}R_{\Gamma}\sigma_{ao} > N\sigma_{NRA} \quad . \tag{33}$$

If a gain of 10 or more per unit length is desired, relation (33) is

$$N^{*}R_{T}(t)\ R_{f}R_{\Gamma}\sigma_{ao} \geq 10N\sigma_{NRA} \quad . \tag{34}$$

Once a reasonable value of N^{*} is chosen, the maximum allowable temperature rise may be calculated. Assuming $N^{*} = 0.1\ N$, relation (34) becomes

$$R_{T}(t)R_{f}R_{\Gamma} \geq 100\ \frac{\sigma_{NRA}}{\sigma_{ao}} \quad . \tag{35}$$

Table VII is a summary of σ_{NRA}/σ_{ao} evaluated from data in Tables I and II.

TABLE VII

σ_{NRA}/σ_{ao} AT 6, 10, AND 15 keV FOR Be, Fe, AND Ta

		E(keV)	
Material	6.0	10.0	15.0
Be	1.14[-5]	6.77[-6]	6.85[-6]
Fe	2.19[-3]	1.34[-2]	9.73[-3]
Ta	3.08[-2]	6.19[-2]	7.52[-2]

Since

$$R_T(t)R_fR_\Gamma \leq 1.0^\dagger \quad , \tag{36}$$

it is required by relation (35) that

$$\frac{\sigma_{NRA}}{\sigma_{ao}} \leq 10^{-2} \quad . \tag{37}$$

Although σ_{NRA}/σ_{ao} is exceedingly low for Be, it must be remembered that Be is only the host material and that N^* refers to the population inversion of the active isotope. Assuming that the concentration of the parent isotope in the Be host is approximately 10^{-4}, then it is required that

$$\frac{\sigma_{NRA}}{\sigma_{ao}} \leq 10^{-6} \quad . \tag{38}$$

This eliminates from consideration all but the 6.0 and 15.0 keV lines.

The variation of σ_{NRA}/σ_{ao} with energy for the case of Fe demonstrates the effect of an absorption edge in the photoelectric cross section. Whether the photon energy is above or below an edge can sometimes determine whether or not a particular transition may be a candidate for the graser application.

Using the 6.0 keV line in some hypothetical material for which $\frac{\sigma_{NRA}}{\sigma_{ao}} = 2.19 \times 10^{-3}$ and $A \sim 60^+$, relation (35) becomes

$$R_T(t)R_fR_\Gamma \geq 0.219 \quad . \tag{39}$$

---

†The case of $R_f > 1.0$ in tungsten boride is considered anomalous.

$^+$For instance, at 6.0 keV $\frac{\sigma_{NRA}}{\sigma_{ao}} = 2.58 \times 10^{-3}$ in Co and at 8.0 keV $\frac{\sigma_{NRA}}{\sigma_{ao}} = 2.26 \times 10^{-3}$ in Ni.

From Table VI,

$$0.33 \leq R_f \leq 1.87 \quad ,$$

$$0.13 \leq R_\Gamma \leq 0.71 \quad ,$$

resulting in $$0.043 \leq R_f R_\Gamma \leq 1.33 \quad . \tag{40}$$

However, it was noted in Sec. 5 that, in general, R_f and R_Γ would be larger for monatomic metals. Therefore, using the entries in Table VI for W, Fe, and Pt, it is noted that $R_f \geq 0.9$ and $R_\Gamma \geq 0.4$, so that a reasonable value for $R_f R_\Gamma$ is

$$R_f R_\Gamma = 0.4 \quad . \tag{41}$$

In this case,

$$R_T(t) \geq 0.55 \quad , \tag{42}$$

implying that,

$$f(T_m) = 0.55^{*} \quad , \tag{43}$$

where T_m is the maximum allowable temperature. Using the Debye approximation in Eq. (4),

$$-\frac{3E^2}{Mc^2 k\theta}\left[\frac{1}{4} + \left(\frac{T}{\theta}\right)^2 \int_0^{\theta/T} \frac{x\,dx}{e^x - 1}\right] = \ln(0.55) = -.602 \quad , \tag{44}$$

---

[*] Although $f_o \neq 1.0$, as used in the calculation of σ_a in Sec. 2.3., it does not affect the calculation of $f(T_m) = R_T(t)$. σ_{ao} should be $\sigma_{ao} = \sigma_a f_o$ so that $R_T(t) \geq 0.55/f_o$, but $R_T(t) \equiv f(T)/f_o$ so that $f(T) = f_o R_T(t) = f_o 0.55/f_o = 0.55$.

or $$\frac{1}{4}+\left(\frac{T}{\theta}\right)^2\int_0^{\theta/T}\frac{xdx}{e^x-1}=5.4\quad, \tag{45}$$

assuming E = 6.0 keV,

M = 60 amu,

θ = 200° K.

Using the high temperature approximation,

$$\frac{1}{4}+\left(\frac{T}{\theta}\right)^2\int_0^{\theta/T}\frac{xdx}{e^x-1}\approx\frac{T}{\theta}\quad, \tag{46}$$

yields $T \approx 5.4\theta \approx 1000°$ K.

Although at such high temperatures the Debye model should not be used to calculate the recoilless fraction, it is nevertheless fair to conclude that a substantial rise in temperature can be tolerated in this case.

6.4. Limitations on the Pumping Flux

Assuming a maximum allowable temperature rise of 1000° K, the maximum allowable average energy of the neutron flux may be calculated. Using the following typical parameters for a medium Z material:

A = 60. grams/mol,

N = 8.5[22] atoms/cm^3,

σ = 3.0 barns,

ρ = 8.5 grams/cm^3,

c = 0.1 cal/gm-°K,

it is found that the energy input, ε, required to raise the temperature of the body by 1000° K is

$$\varepsilon = 1000\rho c = 850 \text{ cal/cm}^3 = 2.22\ [22]\ \text{eV/cm}^3. \tag{48}$$

By Eq. (18),

$$\varepsilon = qt = N\sigma\phi t\chi \quad . \tag{49}$$

According to Ref. 6, even under favorable circumstances a neutron fluence of 10^{19} - 10^{20} n/cm^2 would be required. Assuming $\phi t = 10^{20}$ n/cm^2 results in

$$\chi = 871 \text{ eV/PKA} \quad . \tag{50}$$

In this energy range χ is given by Eq. (19b) so that

$$\overline{E}_n = 54 \text{ keV}^* \quad . \tag{51}$$

A fluence of 10^{20} n/cm^2 with an average energy of 54 keV causes a displacement concentration of ∿ 1% (see Appendix E). Thus the reduction factors used in this analysis are appropriate, and since χ and N_d are linear in E_n in this energy regime and T_m is fixed, the displacement concentration is also fixed. This is a result of the following considerations. If the fluence is increased by some factor, then to keep the temperature rise unchanged, χ must be decreased by this same factor. E_n is also decreased by this factor, since χ is linear in E_n. Since N_d is linear in both E_n and ϕt, N_d remains unchanged.

---

[*] In calculating this average energy, the flux was treated as though it could be replaced by a monoenergetic flux with an energy, E_n, equal to the average energy of the actual flux $\overline{E}_n$. This can only be done for neutron energies less than L_c/Λ, since for neutron energies greater than L_c/Λ, Eqs. (17c) and (19c) are not linear in the neutron energy. Therefore, substituting the average energy for a group of neutrons does not yield the correct result. However, since 54 keV is very much less than L_c/Λ (∿ 775 keV) for a medium-Z material, it can be assumed that very few neutrons have energies above L_c/Λ and little error is introduced.

PART 7

DISCUSSION AND CONCLUSIONS

It is seen from the preceding analysis that the possibility of creating a graser is not negated on the grounds of radiation damage; however, until a particular isomeric transition is chosen, nothing more specific can be said concerning the radiation damage aspects of the problem. Once a particular isomeric transition that appears to satisfy the requirements for the graser is found, a thorough Mössbauer study should be undertaken, including a determination of f and Γ as functions of temperature and damage. If the material exists as a metal, this would probably be the preferred form; however, a study of its compounds is in order.

Since the evidence presented in this paper indicates that $R_f R_\Gamma \gtrsim 0.4$, one may conclude that the gain of a potential graser system is more sensitive to the nuclear parameters of the isomeric transition chosen, than to radiation damage effects. The pumping requirements as estimated by Gol'danskii and Kagan[6] are more stringent than the limitations upon the flux due to radiation damage considerations.

Suggestions that the inverted isotope be ion implanted into a diamond or absorbed into a clathrate may be dismissed on the grounds that the openness of their lattices allows a large $\langle x^2 \rangle$ and, therefore, a small recoilless fraction; so that no advantage is gained by this technique.

PART 8

LITERATURE CITED

1. B. V. Chirikov, "The Kinetics of Induced Mössbauer Radiation," Sov. Phys. JETP 17, 1355 (1963).

2. W. Vali and V. Vali, "Induced Gamma-Ray Emission," Proc. IEEE 51, 182 (1963).

3. G. C. Baldwin, J. P. Neissel, J. H. Terhune, and L. Tonks, "On The Possibility of Maser Action Between Nuclear States," Trans. Am. Nuc. Soc. 6, 178 (1963).

4. G. C. Baldwin, J. P. Neissel, and L. Tonks, "Induced Gamma-Ray Emission," Proc. IEEE 51, 1247 (1963).

5. G. C. Baldwin and J. H. Terhune, "Nuclear Superradiance in Solids," Phys. Rev. Letters 14, 589 (1965).

6. V. I. Gol'danskii and Yu. Kagan, "The Possibility of Creating a Nuclear Gamma Laser," Zh. Eksp. Teor. Fiz. 64, 90 (1973).

7. R. V. Khokhlov, "Concerning the Feasibility of a Gamma Laser Based on Radioactive Crystals," ZhETF Pis. Red. 15, 580 (1972).

8. V. S. Letokhov, "On the Problem of the Nuclear-Transition Gamma-Laser," Zh. Eksp. Teor. Fiz. 64, 1555 (1973).

9. V. V. Kokorin and V. F. Los', "Stimulated Emission of Gamma Rays From Crystals," Fiz. Tverd. Tela 15, 1776 (1973).

10. V. I. Gol'danskii and Yu. M. Kagan, "Feasibility of the Nuclear-Transition Gamma-Laser (Gaser)," Sov. Phys.-Usp. 16, 563 (1974).

11. Yu. A. Il'inskii and R. V. Khokhlov, "The Possibility of Observing Stimulated Gamma Radiation," Sov. Phys.-Usp. 16, 565 (1974).

12. V. I. Gol'danskii, Yu. Kagan, and V.A. Namiot, "Two-Stage Excitation of Nuclei to Obtain Stimulated Gamma-Quantum Emission," ZhETF Pis. Red. 18, 61 (1973).

13. V. A. Bushuev and R. N. Kuz'min, "From the Current Literature," Usp. Fiz. Nauk 114, 677 (1974).

14. G. C. Baldwin, "Is There a High Frequency Limit to Laser Action," in Laser Interaction and Related Plasma Phenomena, Vol.3, H. J. Schwarz and H. Hora, Eds. (Plenum Publishing Corp., New York, 1974), pp. 875-888.

15. G. C. Baldwin, "New Look at the Graser," Laser Focus, pp. 42-47 (March, 1974).

16. G. C. Baldwin, "Research Problems in the Development of Gamma-Ray Lasers," Presented at the 1974 Spring Meeting of the Optical Society of America, Washington, D. C.; see Abstract in Optical Society of America, Journal 64, 556, paper ThA4 (1974).

17. G. C. Baldwin and R. V. Khokhlov, "Prospects for a Gamma-Ray Laser," Physics Today 28, 32 (1975).

18. G. C. Baldwin, J. W. Pettit, and H. R. Schwenn, "Critical Review of Current Proposals for Mössbauer Grasers," Proc. Intern. Conf. Mössbauer Spectroscopy, Cracow, Poland, 1975(Akademia Górniczo-Hutnicza Im. S. Staszica W Krakowie, Krakow, 1975), Vol. 2, pp. 413-428.

19. G. C. Baldwin, "Problems of the Gamma-Ray Laser," BRL Contract Report CR-179 (1974).

20. L. Wood, G. Chapline, S. Slutz, and J. Nuckolls, "X-Ray and Gamma-Ray Laser Studies at the Lawrence Livermore Laboratory," Presented at the 1974 Spring Meeting of the Optical Society of America, Washington, D. C.; see Abstract in Optical Society of America, Journal 64, 556, paper ThA3 (1974).

21. L. Wood and G. Chapline, "Towards Gamma-Ray Lasers," Nature 252, 447 (1974).

22. F. J. Lynch, R. E. Holland, and M. Hamermesh, "Time Dependence of Resonantly Filtered Gamma Rays from Fe^{57}," Phys. Rev. 120, 513 (1960).

23. G. C. Baldwin, "Notes on Graser Seminars," Los Alamos Scientific Laboratory report LA-6853-MS (to be published).

24. P. Hannaford, C. J. Howard, and J. W. G. Wignall, "Effect of Radiation Damage on the 23.8-keV Mössbauer Transition in ^{119}Sn," Physics Letters 19, 257 (1965).

25. W. Mansel, G. Vogl, W. Vogl, H. Wensl, and D. Barb, "Mössbauer Measurements of the Debye-Waller Factor of Gold in Platinum after Low-Temperature Neutron Irradiation," Phys. Status Solidi 40, 461 (1970).

26. G. Vogl, A. Schaefer, W. Mansel, J. Prechtel, and W. Vogl, "Mössbauer Studies of Low-Temperature Radiation Damage in α-Iron," Phys. Status Solidi B 59, 107 (1973).

27. R. Kelly and H. M. Naguib, "Ion-Impact Crystalization of ZrO_2 and Its Implications to Other Materials," in Atomic Collision Phenomena in Solids, D. W. Palmer, M. W. Thompson, and P. D. Townsend, Eds., Proc. of Int. Conf., University of Sussex, Brighton, England, September 7-12, 1967 (Amsterdam, North-Holland; New York, American Elsevier, 1970), pp. 172-191.

28. J. A. Brinkman, "On the Nature of Radiation Damage in Metals," J. Appl. Phys. 25, 961 (1954).

29. F. A. Nichols, "Effects of High Neutron Exposures on Properties of Materials," in Annual Review of Materials Science, Vol. 2, R. A. Huggins, R. H. Bube, and R. W. Roberts, Eds. (Annual Reviews, Inc., Palo Alto, CA, 1972), pp. 463-500.

30. C. Erginsoy, G. H. Vineyard, and A. Englert, "Dynamics of Radiation Damage in a Body-Centered Cubic Lattice," Phys. Rev. 133, A595 (1964); C. Erginsoy, G. H. Vineyard, and A. Shimizu, "Dynamics of Radiation Damage in a Body-Centered Cubic Lattice. II. Higher Energies," Phys. Rev. 139, A118 (1965).

31. J. R. Beeler, Jr., "Displacement Spikes in Cubic Metals. I. α-Iron, Copper, and Tungsten," Phys. Rev. 150, 470-487 (1966).

32. G. H. Kinchin and R. S. Pease, "The Displacement of Atoms in Solids by Radiation," in Reports on Progress in Physics, A. C. Strickland, Ed. (The Physical Society, London, 1955), pp. 1-51.

33. W. S. Snyder, and J. Neufeld, "Disordering of Solids by Neutron Radiation," Phys. Rev. 97, 1636-1646 (1955).

34. G. J. Dienes and G. H. Vineyard, Radiation Effects in Solids (Inter-Science Publishers, Inc., New York, 1957), pp. 24, 42, 67, 79.

35. L. T. Chadderton, Radiation Damage in Crystals, (John Wiley & Sons, Inc., New York, 1965) p. 30.

36. G. K. Wertheim, A. Hausman, and W. Sander, Electronic Structure of Point Defects, Vol. 4 in series, "Defects in Crystalline Solids," S. Amelinckx, R. Gevers, J. Nihoul, Eds. (North-Holland Publishing Company, Amsterdam, 1971), pp. 13-15.

37. J. A. Stone and W. L. Pillinger, "Recoilless Gamma-Ray Emission after Alpha Decay," Phys. Rev. Letters 13, 200-202 (1964).

38. S. L. Ruby and R. E. Holland, "Mössbauer Effect in K^{40} Using an Accelerator," Phys. Rev. Letters 14, 591-593 (1965).

39. D. W. Hafemeister and E. Brooks Shera, "Mössbauer Effect of the 29.4-keV Neutron Capture Gamma Ray of K^{40}," Phys. Rev. Letters 14, 593-595 (1965).

40. D. Seyboth, F. E. Obenshain, and G. Czjzek, "Observation of Recoilless Emission of ^{61}Ni Gamma Rays Following Coulomb Excitation," Phys. Rev. Letters 14, 954-956 (1965).

41. Y. K. Lee, P. W. Keaton, Jr., E. T. Ritter, and J. C. Walker, "Mössbauer Effect from Coulomb-Excited Levels in Fe^{57}," Phys. Rev. Letters 14, 957-958 (1965).

42. J. Fink and P. Kienle, "Recoilless γ Emission in ^{156}Gd and ^{158}Gd Following Neutron Capture Reactions," Phys. Letters 17, 326-327 (1965).

43. D. A. Goldberg, P. W. Keaton, Jr., Y. K. Lee, L. Madansky, and J. C. Walker, "Mössbauer Effect Resulting from the Reaction Fe^{56}(d,p)Fe^{57}," Phys. Rev. Letters 15, 418-419 (1965).

44. C. Czjzek, J. L. C. Ford, Jr., F. E. Obenshain, and D. Seyboth, "Observation of the Mössbauer Effect Following Coulomb Excitation of ^{73}Ge," Phys. Letters 19, 673-675 (1966).

45. E. T. Ritter, P. W. Keaton, Jr., Y. K. Lee, R. R. Stevens, Jr., and J. C. Walker, "Mössbauer Effect Following Coulomb Excitation of Fe^{57}," Phys. Rev. 154, 287-291 (1967).

46. G. Czjzek, J. L. C. Ford, Jr., J. C. Love, F. E. Obenshain, and H. F. Wegener, "Coulomb-Recoil-Implantation Mössbauer Experiments with ^{73}Ge," Phys. Rev. Letters 18, 529-531 (1967); Phys. Rev. 174, 331-345 (1968).

47. W. G. Berger, J. Fink, and F. E. Obenshain, "Observation of the Mössbauer Effect with ^{57}Fe Following Neutron Capture in ^{56}Fe," Phys. Letters 25A, 466-468 (1967).

48. B. H. Zimmermann, H. Jena, G. Ischenko, H. Kilian, and D. Seyboth, "Mössbauer Experiments with Coulomb-Excited ^{73}Ge after Coulomb Recoil Implantation," Phys. Status Solidi 27, 639-651 (1968).

49. K. A. Hardy, D. C. Russell, and R. M. Wilenzick, "Mössbauer Effect Following Coulomb Excitation of ^{183}W," Phys. Letters 27A, 422-423 (1968).

50. C. G. Jacobs, Jr., N. Hershkowitz, and J. B. Jeffries, "Recoil Radiation Damage Following Coulomb Excitation," Phys. Letters, 29A, 498-499 (1969); C. G. Jacobs, Jr., and N. Hershkowitz, "Mössbauer-Effect Observations of Recoil Radiation Damage Following Coulomb Excitation in Various Hf Coumpounds," Phys. Rev. B 1, 839-850 (1970).

51. F. de S. Barros, D. Hafemeister, and P. J. Vicarro, "Mössbauer Study of ^{57}Co Implanted in Diamond," J. Chem. Phys. 52, 2865-2867 (1970).

52. M. W. Mekshes and N. Hershkowitz, "Mössbauer Effect in Tungsten Following Coulomb Excitation," Phys. Rev. C 2, 289-296 (1970).

53. N. Hershkowitz, Private Communication.

54. K. A. Hardy, J. C. Walker, and R. Shnidman, "Observation of Temperature Spikes Following Coulomb Excitation," Phys. Rev. Letters 29, 622-625 (1972).

55. S. A. Wender and N. Hershkowitz, "Long-Lived Reductions in Recoilless Fractions Following Coulomb Excitation," Phys. Rev. Letters 29, 1648-1651 (1972).

56. R. L. Lambe and D. Schroeer, "Coulomb-Excitation Mössbauer Effect in the 21.6 keV State of ^{151}Eu," Phys. Letters 41A, 435-436 (1972).

57. S. A. Wender and N. Hershkowitz, "Recoil Radiation Damage in Tungsten Compounds Observed Using the Mössbauer Effect Following Coulomb Excitation," Phys. Rev. B 8, 4901-4909 (1973).

58. E. W. Rork and P. S. Jastram, "Anomalous Temperature Dependence of Recoilless Emission: ^{161}Dy in Molybdenum," Phys. Rev. Letters 29, 1297-1299 (1972).

59. E. T. Whittaker and G. N. Watson, A Course of Modern Analysis (Cambridge University Press, London, 1940), p. 381.

APPENDIX A

CALCULATION OF $\bar{t}$ AND CASCADE LIFETIME

If the displacement cascade is modeled by a branching sequence of binary collisions with a mean free path of 5 Å between collisions, then the number of atoms involved in each generation of the cascade, as well as the lifetime of each generation, may be estimated as shown in Tables A-1 and A-2.

In these tables line 1 gives i, the generation of the cascade. Line 2 is n_i, the number of atoms involved in the i^{th} generation of the cascade. Line 3 is the average energy of the knock-on atom (in the i^{th} generation), T_i. It is assumed that 25 eV is expended in creating each displacement and that the remaining energy is, on the average, divided evenly between the colliding nuclei; thus,

$$T_{i+1} = (T_i - 25)/2 \text{ eV} \quad . \qquad \text{(A-1)}$$

The average energy of the primary knock-on atom (PKA), T_1, is determined by the neutron energy according to the equation,

$$T_1 = \frac{1}{2}\Lambda E_n - 25 \text{ eV} \quad . \qquad \text{(A-2)}$$

For a crystal composed of atoms of atomic weight A = 60 (as considered in Table A-1) and a neutron energy of 1 MeV, the energy of the PKA is

$$T_1 = 3.2\ [4] \text{ eV} \quad .$$

For A = 180 (Table A-2),

$$T_1 = 1.1\ [4] \text{ eV} \quad .$$

Line 4 is the velocity of the knock-on, v_i, corresponding to the energy T_i. Line 5 is the time, t_i, a knock-on of velocity v_i takes to traverse 5 Å. This is the lifetime of the i^{th} generation. Line 6 is $\sum_{j=1}^{i} t_j$, the total elapsed time (from the formation of the PKA) through the i^{th} generation.

The branching sequence proceeds until the energy of the knock-ons drops below 25 eV, at which point no further displacements may be formed. This occurs after the 11th generation in Table A-1 and after the 9th generation in Table A-2. At this point the displacements already in motion continue to scatter through the crystal, losing half of their energy with each collision, until their energy drops below 1 eV, at which time they are assumed to be captured (as interstitials).

It may be noticed that Table A-1 predicts 1024 displacements and Table A-2 predicts 256 displacements while the Kinchin and Pease model predicts 645 and 220 displacements, respectively. This discrepancy occurs because of the crude model used here to generate Table A-1 and A-2. Looking at Table A-1 in particular, it is seen that the 512 knock-ons of the 10th generation move off with an energy of 38 eV. In the next set of collisions (with the knock-ons of the 11th generation) not every collision may produce a displacement, as assumed in the model used to generate these tables. Some of the collisions will transfer less than 25 eV to the knock-ons; thus each collision does not always produce a displacement and the number of displacements does not always double with each generation. Therefore, the model of Kinchin and Pease will continue to be used to calculate ν; however, Tables A-1 and A-2 are adequate to estimate the lifetime of a collision cascade and $\bar{t}$, the average moving lifetime of a knock-on.

From Tables A-1 and A-2 the lifetime of a cascade is seen to be on the order of 10^{-12} s. The average moving lifetime of a knock-on, $\bar{t}$, is given by

$$\bar{t} = \sum_j n_j t_j / \nu \quad .$$

For Table A-1,

$$\sum_j n_j t_j = 8.46\ [-10] \quad ;$$

then, using $\nu = 1024$ as predicted by Table A-1,

$$\bar{t} = 8.26\ [-13]\ \mathrm{s} \quad .$$

If $\nu = 645$, as predicted by the model of Kinchin and Pease, then

$$\bar{t} = 1.31\ [-12]\ \mathrm{s} \quad .$$

For Table A-2,

$$\sum_j n_j t_j = 5.05\ [-10]\ \mathrm{s} \quad .$$

using $\nu = 256$ as predicted in Table A-2,

$$\bar{t} = 1.97\ [-12]\ \mathrm{s} \quad .$$

If $\nu = 220$, as predicted by the model of Kinchin and Pease, then

$$\bar{t} = 2.30\ [-12]\ \mathrm{s} \quad .$$

TABLE A-1

i	1	2	3	4	5	6	7	8	9	10	11	12	13	14
n_i	1	2	4	8	16	32	64	128	256	512	1024	1024	1024	1024
T_i eV	3.22[4]	1.61[4]	8.04[3]	4.01[3]	1.99[3]	9.83[2]	4.79[2]	2.27[2]	1.01[2]	3.80[1]	6.49[0]	3.25[0]	1.62[0]	8.12[-1]
v_i cm/s	3.22[7]	2.28[7]	1.61[7]	1.13[7]	8.00[6]	5.62[6]	3.92[6]	2.70[6]	1.80[6]	1.11[6]	4.57[5]	3.23[5]	2.28[5]	1.62[5]
t_i s	1.55[-15]	2.20[-15]	3.11[-15]	4.41[-15]	6.25[-15]	8.90[-15]	1.27[-14]	1.85[-14]	2.78[-14]	4.52[-14]	1.09[-13]	1.55[-13]	2.19[-13]	3.10[-13]
$\sum_{j=1}^{i} t_j$ s	1.55[-15]	3.75[-15]	6.86[-15]	1.13[-14]	1.75[-14]	2.64[-14]	3.92[-14]	5.77[-14]	8.54[-14]	1.31[-13]	2.40[-13]	3.95[-13]	6.14[-3]	9.23[-13]

TABLE A-2

i	1	2	3	4	5
n_i	1	2	4	8	16
T_i eV	1.10[4]	5.47[3]	2.72[3]	1.35[3]	6.62[2]
v_i cm/s	1.08[7]	7.66[6]	5.40[6]	3.80[6]	2.66[6]
t_i s	4.61[-15]	6.53[-15]	9.26[-15]	1.32[-14]	1.88[-14]
$\sum_{j=1}^{i} t_j$ s	4.61[-15]	1.11[-14]	2.04[-14]	3.36[-14]	5.23[-14]

i	6	7	8	9	10
n_i	32	64	128	256	256
T_i eV	3.18[2]	1.47[2]	6.08[1]	1.79[1]	8.96[0]
v_i cm/s	1.85[6]	1.25[6]	8.08[5]	4.38[5]	3.10[5]
t_i s	2.71[-14]	3.99[-14]	6.19[-14]	1.14[-13]	1.61[-13]
$\sum_{j=1}^{i} t_j$ s	7.94[-14]	1.19[-13]	1.81[-13]	2.95[-13]	4.57[-13]

i	11	12	13	14
n_i	256	256	256	256
T_i eV	4.48[0]	2.24[0]	1.12[0]	5.60[-1]
v_i cm/s	2.19[5]	1.55[5]	1.10[5]	7.75[4]
t_i s	2.28[-13]	3.23[-13]	4.56[-13]	6.45[-13]
$\sum_{j=1}^{i} t_j$ s	6.85[-13]	1.01[-12]	1.46[-12]	2.11[-12]

APPENDIX B

DERIVATION OF EQUATION (22)

The differential equation to be solved is

$$\frac{\partial T}{\partial t} = \frac{k}{\rho c} \nabla^2 T + \frac{q}{\rho c} \quad , \qquad \text{(B-1)}$$

for a cylindrical body with initial and boundary conditions:

1) $T(r,0) = 0$, (B-2)

2) $T(R,t) = T_1 = 0$, (B-2b)

3) $\frac{\partial T}{\partial r}(0,t) = 0$. (B-2c)

The solution is assumed to take the form

$$T(r,t) = T_{ss}(r) + T_{tr}(r,t) \quad , \qquad \text{(B-3)}$$

where T_{ss} is a steady state solution and T_{tr} is a transient solution.

The Steady State Solution

$$\frac{\partial T_{ss}}{\partial t} = 0 \; , \qquad \text{(B-4)}$$

so that Eq. (B-1) may be written as

$$q = -k\nabla^2 T_{ss} = -k\left(\frac{d^2 T_{ss}}{dr^2} + \frac{1}{r}\frac{dT_{ss}}{dr}\right) , \qquad \text{(B-5)}$$

in cylindrical coordinates.

Equation (B-5) may be rewritten as

$$-\frac{qr}{k} = rT_{ss}'' + T_{ss}' = (rT_{ss}')' \quad , \qquad \text{(B-6)}$$

where T' indicates differentiation of T with respect to r. Assuming q to be a constant, the solution to Eq. (B-6) is

$$T_{ss} = -\frac{qr^2}{4k} + C_1 \ln r + C_2 \quad .$$

Applying the boundary conditions Eqs. (B-2b) and (B-2c), it is found that

$$C_1 = 0 \quad ,$$

$$C_2 = \frac{qR^2}{4k} \quad ,$$

so that

$$T_{ss}(r) = \frac{q}{4k}(R^2 - r^2) \quad .$$

<u>The Transient Solution</u>

The transient solution may now be determined by transposing the initial and boundary conditions according to the relation:

$$T_{tr}(r,t) = T(r,t) - T_{ss}(r) \quad ,$$

so that

$$T(r,0) = 0 \longrightarrow T_{tr}(r,0) = -\frac{q}{4k}(R^2 - r^2) \quad , \tag{B-7a}$$

$$T(R,t) = 0 \longrightarrow T_{tr}(R,t) = 0 \quad , \tag{B-7b}$$

$$\frac{\partial T}{\partial t}(0,t) = 0 \longrightarrow \frac{\partial T_{tr}}{\partial r}(0,t) = 0 \quad . \tag{B-7c}$$

Substitution of Eq. (B-3) into Eq. (B-1) yields

$$\rho c\left(\frac{\partial T_{ss}}{\partial t} + \frac{\partial T_{tr}}{\partial t}\right) = k\nabla^2 T_{ss} + k\nabla^2 T_{tr} + q \quad . \tag{B-8}$$

Since $\frac{\partial T_{ss}}{\partial t} = 0$,

and $k\nabla^2 T_{ss} + q = 0$,

Equation (B-8) may now be written as

$$\rho c \frac{\partial T_{tr}}{\partial t} = k\nabla^2 T_{tr} \quad . \tag{B-9}$$

If T_{tr} is assumed to be separable, so that

$$T_{tr} = \mathcal{T}(t)\mathcal{R}(r) \quad ,$$

Equation (B-9) may be written as

$$\frac{\rho c}{k} \mathcal{R} \frac{\partial \mathcal{T}}{\partial t} = \mathcal{T}\nabla^2 \mathcal{R}. \tag{B-10}$$

If ρ, c, and k are constant, so that

$$\frac{\rho c}{k} = \text{constant} \equiv \frac{1}{\alpha} \quad ,$$

Equation (B-10) becomes

$$\frac{1}{\alpha} \frac{\partial \mathcal{T}/\partial t}{\mathcal{T}} = \frac{\nabla^2 \mathcal{R}}{\mathcal{R}} = -\lambda^2 \quad . \tag{B-11}$$

<u>Solving for $\mathcal{T}(t)$</u>

Equation (B-11) may be separated as follows:

$$\frac{1}{\alpha} \frac{\partial \mathcal{T}/\partial t}{\mathcal{T}} = -\lambda^2 \quad . \tag{B-12}$$

The solution to (B-12) is

$$\mathcal{T}(t) = C_1 e^{-\alpha\lambda^2 t} \quad . \tag{B-13}$$

<u>Solving for $\mathcal{R}(r)$</u>

Separating Eq. (B-11) also yields

$$\nabla^2 \mathcal{R} = -\lambda^2 \mathcal{R} \quad , \tag{B-14}$$

which may be written in cylindrical coordinates as

$$r^2 \frac{d^2R}{dr^2} + r\frac{dR}{dr} + (\lambda^2 r^2 - 0)R = 0 \quad . \tag{B-15}$$

Performing the change of variables,

$$\mu = \lambda r \quad ,$$

allows Eq. (B-15) to be written as

$$\mu^2 \frac{d^2R}{d\mu^2} + \mu\frac{dR}{d\mu} + (\mu^2 - 0)R = 0 \quad , \tag{B-16}$$

which has the solution:

$$R(r) = C_2 J_o(\lambda r) + C_3 Y_o(\lambda r) \quad . \tag{B-17}$$

The transient solution may now be written as

$$T_{tr} = C_1 e^{-\alpha\lambda^2 t}[C_2 J_o(\lambda r) + C_3 Y_o(\lambda r)] \quad . \tag{B-18}$$

Now the transposed initial and boundary conditions, Eqs. (B-7a, b, and c) are applied to Eq. (B-18).

Eq. (B-7c) implies that

$$C_3 = 0 \quad ,$$

so that

$$T_{tr} = C_1 e^{-\alpha\lambda^2 t}[C_2 J_o(\lambda r)] \quad ,$$

which may be written as

$$T_{tr} = C_4 e^{-\alpha\lambda^2 t} J_o(\lambda r) \quad ,$$

for ease of handling.

Equation (B-7b) implies that

$$J_o(\lambda R) = 0 \quad .$$

Letting the zeroes of J_o be given by ξ_n, so that

$$J_o(\xi_n) = 0 \quad ,$$

permits the allowable values of λ to be determined from the equation,

$$\lambda_n = \frac{\xi_n}{R} \quad .$$

The transient solution may now be written as

$$T_{tr} = \sum_n e^{-\alpha\lambda_n^2 t} C_n J_o(\lambda_n r) \quad .$$

Equation (B-7a) requires that

$$T_{tr}(r,0) = -\frac{q}{4k}(R^2 - r^2) = \sum_n C_n J_o(\lambda_n r) \quad . \tag{B-19}$$

Using the result[59] that

$$A_n = 8[a\lambda_n^3 J_1(\lambda_n a)]^{-1} \quad , \tag{B-20a}$$

in the expansion:

$$a^2 - x^2 = A_1 J_o(\lambda_1 x) + A_2 J_o(\lambda_2 x) + \ldots\ldots \quad , \tag{B-20b}$$

where λ_1, λ_2, etc. are the (+) roots of $J_o(\lambda a) = 0$, allows Eq. (B-19) to be solved by comparison.

Equation (B-19) may be written in the form

$$R^2 - r^2 = \frac{C_1}{-q/4k} J_o(\lambda_1 r) + \frac{C_2}{-q/4k} J_o(\lambda_2 r) + \ldots \quad . \qquad \text{(B-21)}$$

Comparison of Eq. (B-21) to Eq. (B-20b) yields

$$A_n = \frac{C_n}{-q/4k} \quad , \qquad \text{(B-22)}$$

so that

$$C_n = -\frac{q}{4k} A_n = -\frac{q}{4k} \left\{ 8[R\lambda_n^3 J_1(\lambda_n R)]^{-1} \right\} \quad . \qquad \text{(B-23)}$$

Thus

$$T_{tr}(r,t) = \sum_n e^{-\alpha\lambda_n t} \left\{ \frac{-q}{4k} 8[R\lambda_n^3 J_1(\lambda_n R)]^{-1} \right\} J_o(\lambda_n r) \quad . \qquad \text{(B-24)}$$

The complete solution to Eq. (B-1) is, therefore,

$$T(r,t) = \frac{q}{4k} \left\{ (R^2 - r^2) - 8 \sum_n e^{-\alpha\lambda_n^2 t} [R\lambda_n^3 J_1(\lambda_n R)]^{-1} J_o(\lambda_n r) \right\} \quad . \qquad \text{(B-25)}$$

APPENDIX C

CALCULATION OF THE CONCENTRATION OF MOVING KNOCK-ONS

As shown in Appendix A, $\Sigma n_i t_i$ = 8.46 [-10]s for A = 60 (and $\Sigma n_i t_i$ = 5.05 [-10]s for A = 180). Assuming the following parameters:

N_o = 8.5 [22] atoms/cm^3,

σ = 3.0 barns,

ϕ = 1.0 [25] n/cm^2-s,

E_n = 1.0 MeV,

$D_m = N_o \sigma \phi \Sigma n_i t_i$ = 2.16 [15].

The fraction of the crystal atoms in motion is

$$\frac{D_m}{N_o} = \frac{2.16\ [15]}{8.5\ [22]} = 2.54\ [-8]\quad .$$

APPENDIX D

CALCULATION OF THE CONCENTRATION OF DISPLACEMENTS DUE TO 5×10^{18} n/cm^2 ON Fe

Vogl, et al.[26] irradiated an α-iron sample with $\sim 5.2 \times 10^{18}$ fast-n/cm^2, which was then used as a Mössbauer absorber foil. Assuming the following parameters:

$N_o = 8.5$ [22] atoms/cm^2,

$\sigma = 3.0$ barns,

$\phi t = 5.2 \times 10^{18}$ n/cm^2,

$\overline{E}_n = 1$ MeV,

$L_c = 50$ keV,

the number of displacements per PKA, as given by Eq. (15), is

$$\nu = (2 - \frac{L_c}{\Lambda E_n}) \frac{L_c}{4E_d} = 631 \quad .$$

The density of displacements, as given by Eq. (16a), is

$$N_d = N_o \sigma \phi t \nu = 8.37\ [20] \quad ,$$

which is

$$\frac{N_d}{N_o} \times 100\% = 0.99\% \sim 1\ \% \text{ of the crystal.}$$

APPENDIX E

CALCULATION OF THE CONCENTRATION OF DISPLACEMENTS DUE TO THE CALCULATED ALLOWABLE FLUENCE

The relative displacement concentration, $[N_d]$, is given by

$$[N_d] = \frac{N_d}{N_o} \quad ;$$

so that Eq. (16a) becomes

$$[N_d] = \sigma\phi t\nu \quad .$$

By Eq. (17b)

$$\nu = \frac{\Lambda E_n}{4E_d} \quad .$$

Substituting the values:

$\sigma = 3$ barns,

$\phi t = 1\ [20]\ n/cm^2$,

$E_n = 54$ keV,

yields

$$[N_d] = 0.01 \quad .$$

ACKNOWLEDGEMENTS

During the research and writing of this thesis, I have received the help, guidance, and support of many people. To the cast of literally tens who participated or in some way influenced this work, I want to say thank you. In particular, I wish to express my appreciation to my thesis adviser, Dr. G. C. Baldwin, for his encouragement and guidance throughout the period of this research. Technical discussions with Dr. H. B. Huntington were always illuminating and helpful, and are gratefully acknowledged as is financial support from the Los Alamos Scientific Laboratory. I want to thank all the members of Group P-3 (LASL) for their friendship, hospitality, and professional guidance during my visits. I would also like to thank Drs. C. E. Ragan III and J. C. Solem for their reading of the manuscript and their many helpful suggestions. I am especially grateful to Mrs. Carol Myers for her dedication in preparing the typed manuscript.

I cannot adequately express my gratitude to Dr. G. A. Keyworth II for making my visits to P-3 possible, for taking it upon himself to make a physicist of me, and for the many enlightening discussions.